Lawrence Berkeley National Laboratory
LBL Publications

Title
Investigating the role of tetraquark operators in lattice QCD studies of the a0(980) and κ resonances

Permalink
https://escholarship.org/uc/item/3n23478x

Journal
Physical Review D, 114(1)

ISSN
2470-0010

Authors
Hanlon, Andrew D
Darvish, Daniel
Skinner, Sarah
et al.

Publication Date
2026-07-01

DOI
10.1103/bs45-shv9

Copyright Information
This work is made available under the terms of a Creative Commons Attribution License, available at https://creativecommons.org/licenses/by/4.0/

Peer reviewed

eScholarship.org Powered by the California Digital Library
University of California

Investigating the role of tetraquark operators in lattice QCD studies of the $a_0(980)$ and κ resonances

Andrew D. Hanlon,[1,*] Daniel Darvish,[2] Sarah Skinner,[2] John Meneghini,[2] Ruairí Brett,[2] John Bulava,[3] Jacob Fallica,[2] Colin Morningstar,[2] Fernando Romero-López,[4] and André Walker-Loud[5]

[1]*Department of Physics, Kent State University, Kent, Ohio 44242, USA*
[2]*Department of Physics, Carnegie Mellon University, Pittsburgh, Pennsylvania 15213, USA*
[3]*Fakultät für Physik und Astronomie, Institut für Theoretische Physik II, Ruhr-Universität Bochum, 44780 Bochum, Germany*
[4]*Institute for Theoretical Physics, Albert Einstein Center for Fundamental Physics, University of Bern, 3012 Bern, Switzerland*
[5]*Nuclear Science Division, Lawrence Berkeley National Laboratory, Berkeley, California 94720, USA*

(Received 20 March 2026; accepted 12 June 2026; published 23 July 2026)

The role of tetraquark operators in studying the isodoublet strange κ and isovector nonstrange $a_0(980)$ scalar mesons in lattice quantum chromodynamics (QCD) is examined using an ensemble with $m_\pi \approx 230$ MeV and spatial extent L such that $m_\pi L \approx 4.4$. Hermitian correlation matrices using both single-meson, meson-meson, and tetraquark interpolating operators are used to extract the spectrum of finite-volume stationary states in the appropriate symmetry channels. Hundreds of local and extended tetraquark operators are explored. Determinations of the spectrum in each channel are found to be unreliable without the inclusion of at least one tetraquark operator. For example, the inclusion of tetraquark operators with isospin $1/2$ and strangeness 1 quantum numbers reveals the existence of an additional energy level in the $K\eta$ subsystem below the $K\eta$ threshold. The implications of this on parametrizing the scattering K-matrix through a well-known quantization condition to extract properties of the κ and $a_0(980)$ scalar meson resonances are discussed.

DOI: 10.1103/bs45-shv9

I. INTRODUCTION

The low-lying scalar mesons of quantum chromodynamics (QCD) present significant challenges to experimental and theoretical studies compared to other hadrons. The large decay widths of the scalar resonances make them difficult to resolve from background processes in scattering experiments, with multiple decay channels opening up within small energy ranges. The scalar mesons defy description by the naive quark model [1,2]. These systems are also difficult to study in lattice QCD, requiring correlation matrices which involve a large variety of different interpolating operators and whose evaluations are hampered by noisy fermionic disconnected contributions.

It has been suggested that the $a_0(980)$ and $K_0^*(700)$ (also known as the κ) scalar resonances could have tetraquark content [3–6]. Tetraquark operators have been shown [7–9] to be important for the $T_{cc}(3875)^+$ resonance. To date, there has been only a small number of lattice QCD studies investigating the tetraquark content of light scalar resonances. In 2010, Prelovsek *et al.* [10] investigated the σ and κ as possible tetraquark candidates, but neglected disconnected diagrams in their calculations. Using tetraquark interpolators, they found an additional light state in both the σ and κ channels. In 2013, the ETM collaboration examined the $a_0(980)$ and κ using four-quark operators [11], though they also neglected disconnected diagrams in their calculations. They found no evidence of an additional state that can be interpreted as a tetraquark. In 2018, Alexandrou *et al.* [12] conducted a study of the $a_0(980)$ with four-quark operators, including disconnected contributions. In their study, they found an additional finite-volume state in the sector containing the $a_0(980)$ meson, which has primarily quark-antiquark content but also has sizeable diquark-antidiquark content, in the range of 1100 to 1200 MeV. Additionally, they concluded that disconnected diagrams have drastic effects on their results, and thus, cannot be neglected. The importance of including disconnected diagrams when studying the κ and $a_0(980)$ (as well as other scalar mesons) is also shown in Ref. [13].

In this work, we examine the role of tetraquark operators in lattice QCD studies of the $a_0(980)$ and κ scalar meson

*Contact author: ahanlon7@kent.edu

Published by the American Physical Society under the terms of the Creative Commons Attribution 4.0 International license. Further distribution of this work must maintain attribution to the author(s) and the published article's title, journal citation, and DOI. Funded by SCOAP³.

resonances. We make two different determinations of the spectrum in each symmetry sector: one using a basis of only single- and two-meson operators, and one using a basis that also includes a tetraquark operator selected from hundreds of tetraquark operators which were tested in preliminary low-statistics Monte Carlo calculations. The stochastic LapH method [14] is used to evaluate the diagrams in our calculations, including *all* disconnected contributions. We find that including a tetraquark operator yields an additional low-lying finite-volume state in the isodoublet strange A_{1g} sector. In the $a_0(980)$ channel, a significant change in the extracted spectrum occurs upon inclusion of the tetraquark operator.

To obtain hadron scattering amplitudes and resonance information in lattice QCD, the first step is to compute the energies of the finite-volume (FV) stationary states in the relevant channels of interest involving the scattered hadrons. Once the FV spectra are obtained, the elements of the infinite-volume scattering K matrix must be appropriately parametrized, then best fit values of the parameters are obtained using an appropriate quantization condition [15–18]. In this exploratory work, we focus mainly on the first step, extracting the FV spectra, highlighting the importance of using judiciously chosen interpolating operators. In Sec. II, we describe our lengthy exploration of interpolating operators and find that at least one tetraquark operator seems to be necessary for reliably extracting all of the needed energies of the FV spectra relevant for lattice QCD studies of the κ and $a_0(980)$ resonances. Our results for the FV spectra are then presented in Sec. III. In Sec. IV, we address the impact of the tetraquark operators on determining the K-matrix parameters, followed by concluding remarks in Sec. V.

II. INTERPOLATING OPERATORS

The interpolating operators we use to determine the low-lying energies of the stationary states of QCD in finite volume in the isodoublet strange A_{1g} and isotriplet non-strange A_{1g}^- channels of total zero momentum are described in this section. First, we describe how we obtain these energies from matrices of temporal correlations of interpolating operators in Sec. II A. The construction of our single-meson and two-meson operators is then outlined in Sec. II B, and our construction of hundreds of tetraquark operators is detailed in Sec. II C. Calculation details, such as the parameters of our ensemble of gauge configuration, our gluon and quark field smearing, and our use of the stochastic LapH method, are outlined in Sec. II D. The final sets of interpolating operators to use are presented in Sec. II E, along with an outline of the procedure used to select them.

A. Energies from temporal correlations

In lattice QCD, the energies of the stationary states in finite volume are extracted from matrices of temporal correlations

$$\mathcal{C}_{ij}(t) = \langle 0|O_i(t+t_s)\bar{O}_j(t_s)|0\rangle, \tag{1}$$

where t is the time separation, t_s is some reference source time, and $O_i(t)$ denotes the ith interpolating operator constructed from quark and gluon fields to annihilate single- and multihadron states having appropriate transformation properties. The corresponding creation operators are denoted by $\bar{O}_i(t)$. The operators O_i and $\bar{O}_i$ are the analytic continuations to Euclidean space of the Minkowski-space operators $O_i^{(M)}$ and $O_i^{(M)\dagger}$, respectively. In the imaginary time formalism, estimates of these $\mathcal{C}_{ij}(t)$ correlators can be obtained using a Markov-chain Monte Carlo method. The various diagonal elements of this matrix at early times can differ drastically in magnitude due to different operator normalizations. To ameliorate any possible numerical instabilities from these physically irrelevant normalizations, the following rescaled matrix is formed and subsequently used

$$C_{ij}(t) = \frac{\mathcal{C}_{ij}(t)}{\sqrt{\mathcal{C}_{ii}(t_N)\mathcal{C}_{jj}(t_N)}}, \tag{2}$$

where the normalization time $t_N = \tau_N a_t$ is taken at some early time, such as $t_N < 3a_t \sim 0.1$ fm, and a_t is the temporal lattice spacing. In finite volume, the stationary-state energies E_n are discrete, so by inserting a complete set of states, these correlators can be expressed in terms of the energies using

$$C_{ij}(t) = \sum_{n=0} Z_i^{(n)} Z_j^{(n)*} e^{-E_n t}, \qquad Z_j^{(n)} = \langle 0|O_j|n\rangle, \tag{3}$$

ignoring negligible effects from the temporal boundary and taking $E_{n+1} \geq E_n$.

Given the large number of complex-valued overlap factors $Z_i^{(n)}$ in Eq. (3), it is not practical to do simultaneous fits to the entire $C(t)$ matrix to determine the low-lying energies, so instead, separate fits are carried out to each of the diagonal elements of the matrix $\tilde{C}(t)$ obtained using a single-pivot rotation [19–21]

$$\tilde{C}(t) = U^\dagger C(t_0)^{-1/2} C(t) C(t_0)^{-1/2} U, \tag{4}$$

where the columns of the unitary matrix U are the orthonormal eigenvectors of $C(t_0)^{-1/2}C(t_D)C(t_0)^{-1/2}$, determined by solving a generalized eigenvector problem (GEVP) given by $C(t_D)W = C(t_0)W\Lambda$, where the matrix $W = C(t_0)^{-1/2}U$ and Λ is the diagonal matrix of eigenvalues. We choose $t_0 = \tau_0 a_t$ and $t_D = \tau_D a_t$ large enough so that $\tilde{C}(t)$ remains diagonal within statistical errors for $t > t_D$ and such that the extracted energies are insensitive to increases in these parameters. Typically, two-exponential fits of the form $A_\alpha e^{-E_\alpha t}(1 + B_\alpha e^{-\Delta t})$ to the diagonal elements $\tilde{C}_{\alpha\alpha}(t)$ yield the energies E_α, and the magnitudes of the overlap factors are determined using $|Z_j^{(n)}| = |C(t_0)_{jk}^{1/2} U_{kn} A_n^{1/2}|$ (no sum over n). Such fits are done

using the standard correlated-χ^2 method with the full covariance matrix of the correlator estimates in the χ^2 evaluated by bootstrap resampling and the fit parameter uncertainties estimated by bootstrap resampling.

Since stochastic estimates of $C_{ij}(t)$ are obtained using the Monte Carlo method and the signal-to-noise ratios of such estimates fall quickly with t, it is very important to use judiciously constructed operators $O_j(t)$ to maximize the $|Z_j^{(n)}|$ factor magnitudes for the states of interest and minimize those for unwanted higher-lying states in order to reliably extract the low-lying energies. If the N lowest-lying energies in a particular symmetry channel are needed, a correlation matrix using at least N interpolating operators must be evaluated. To improve the energy extractions, more than N operators are usually required to help remove contamination from levels above the lowest N states. A crucial point, however, is that in practice, for each of the N lowest-lying energies, an operator should be present which produces a state having significant overlap with the eigenstate associated with that energy. Without such an operator set, the limited temporal range of the correlations which can be reliably estimated due to the limited statistics possible with current Monte Carlo methods can lead to missed energy levels.

For each symmetry channel of interest specified by a total momentum and an irreducible representation (irrep) of its little group, a basic set of operators to use should include operators that contain the incoming particles as well as operators that contain the outgoing particles of the scattering process in all of the allowed individual momenta and in spin/orbital combinations that transform according to the irrep of the channel. Determining if *other* operators are also needed and what those operators should be is an important issue.

B. Meson and meson-meson operator construction

Our meson and meson-meson operator construction is detailed in Refs. [22,23], but key points are summarized here. Individual hadron operators are constructed by combining basic building blocks, which are covariantly displaced LapH-smeared quark fields [14] with stout link smearing [24]. The smeared quark field for flavor A is here denoted by $\tilde{\psi}^{(A)}_{a\alpha}(x)$, where a is a color index, α is a Dirac spin index, and x is a lattice site. The gauge-covariantly displaced, LapH-smeared quark fields are formed using

$$q^A_{a\alpha j} = (D^{(j)}\tilde{\psi})^{(A)}_{a\alpha}, \qquad \bar{q}^A_{a\alpha j} = (\tilde{\bar{\psi}}\gamma_4 D^{(j)\dagger})^{(A)}_{a\alpha}, \tag{5}$$

where γ_4 is the temporal Dirac γ-matrix, and $D^{(j)}$ is a gauge-covariant displacement of type j. The displacement type is a sequence of p spatial directions on the lattice $j = (j_1, j_2, \ldots, j_p)$. This displacement can be trivial ($j = 0$ meaning no displacement), a displacement in a given single spatial direction on the lattice by some number of links (typically two or three), or a combination of two or more spatial lattice directions. If we define $d_r = \hat{j}_1 + \hat{j}_2 + \cdots + \hat{j}_{r-1}$, then the displacement $D^{(j)}$ is defined as a product of smeared link variables

$$D^{(j)}(x,x') = \tilde{U}_{j_1}(x)\tilde{U}_{j_2}(x+d_2)\tilde{U}_{j_3}(x+d_3)\ldots \times \tilde{U}_{j_p}(x+d_p)\delta_{x',x+d_{p+1}}. \tag{6}$$

The use of γ_4 in Eq. (5) is convenient for obtaining baryon correlation matrices that are Hermitian.

To construct our meson operators, we first form so-called *elemental* mesonic operators. Such an operator which destroys a state of three-momentum $\boldsymbol{p}$ is given by

$$\Phi^{AB}_{\alpha\beta}(t) = \sum_{\boldsymbol{x}} e^{-i\boldsymbol{p}\cdot(\boldsymbol{x}+\frac{1}{2}(\boldsymbol{d}_\alpha+\boldsymbol{d}_\beta))}\delta_{ab}\bar{q}^A_{a\alpha}(\boldsymbol{x},t)q^B_{b\beta}(\boldsymbol{x},t), \tag{7}$$

where $q, \bar{q}$ are defined in Eq. (5), $\boldsymbol{d}_\alpha$, $\boldsymbol{d}_\beta$ are the spatial displacements of the $\bar{q}, q$ fields, respectively, from $\boldsymbol{x}$, A, B indicate flavor, and α, β are compound indices incorporating both spin and quark-displacement types. The phase factor involving the quark-antiquark displacements is needed to ensure proper transformation properties under G-parity for arbitrary displacement types. The "barred" operators which create a state of momentum $\boldsymbol{p}$ then take the form

$$\bar{\Phi}^{AB}_{\alpha\beta}(t) = \sum_{\boldsymbol{x}} e^{i\boldsymbol{p}\cdot(\boldsymbol{x}+\frac{1}{2}(\boldsymbol{d}_\alpha+\boldsymbol{d}_\beta))}\delta_{ab}\bar{q}^B_{b\beta}(\boldsymbol{x},t)q^A_{a\alpha}(\boldsymbol{x},t). \tag{8}$$

Each meson sink operator is then a superposition of these elemental operators

$$M_l(t) = c^{(l)}_{\alpha\beta}\Phi^{AB}_{\alpha\beta}(t), \tag{9}$$

(or is a flavor combination of the above form), where l is a compound index comprised of a three-momentum $\boldsymbol{p}$, an irreducible representation Λ of the little group of $\boldsymbol{p}$, the row λ of the irrep, total isospin I, isospin projection I_3, strangeness S, and an identifier labeling the different operators in each symmetry channel. The superposition coefficients are determined using group-theoretical projections. The corresponding source operators are

$$\bar{M}_l(t) = c^{(l)*}_{\alpha\beta}\bar{\Phi}^{AB}_{\alpha\beta}(t). \tag{10}$$

The spatial configurations we use for our single meson operators are shown in Table I of Ref. [23]. We use single-site meson operators (SS), singly displaced (SD), doubly displaced in an L-shape (DDL), and triply displaced in a U-shape (TDU) and using three orthogonal directions (TDO). For mesons having nonzero momenta, quark displacements can be either transverse or longitudinal to the meson momentum. The flavor structures of our single meson operators are presented in Table I.

TABLE I. Flavor content of our meson annihilation operators. Ordering of the quark/antiquark fields is the same as the annihilation operators shown in Eq. (7). The names $\tilde{\eta}$ and $\tilde{\phi}$ are used to denote $\bar{u}u + \bar{d}d$ and $\bar{s}s$ elemental operators, respectively, to simplify notation; they are not meant to indicate physical η and ϕ meson operators which would be superpositions of $\bar{u}u + \bar{d}d$ and $\bar{s}s$ elementals.

Operator name	Flavor content
π^+	$\bar{d}u$
π^0	$(\bar{d}d - \bar{u}u)/\sqrt{2}$
π^-	$-\bar{u}d$
$\tilde{\eta}$	$\bar{u}u + \bar{d}d$
$\tilde{\phi}$	$\bar{s}s$
K^+	$\bar{s}u$
K^0	$\bar{s}d$
$\bar{K}^0$	$\bar{d}s$
$\bar{K}^-$	$-\bar{u}s$

Our hadron operator construction generalizes to two, three, or more hadrons. To form a two-meson operator $\mathcal{O}_l(t)$, we follow a similar procedure and project the product of two final meson operators $M^a_{l_a}(t)M^b_{l_b}(t)$ onto a final symmetry channel l: $\mathcal{O}_l(t) = c^{(l)}_{l_a l_b} M^a_{l_a}(t)M^b_{l_b}(t)$.

C. Tetraquark operator construction

As previously mentioned, some past works have suggested that the κ and $a_0(980)$ resonances might require tetraquark operators to be investigated reliably [10,12]. To test this, we designed and implemented a large variety of tetraquark operators.

Quark fields at each lattice site x transform under a local gauge transformation (color rotation) according to the fundamental 3 irrep of $SU(3)$, whereas antiquark fields transform according to the complex-conjugate $\bar{3}$ irrep. Color singlet tetraquark operators can be built from the product of two 3 and two $\bar{3}$ objects

$$3 \otimes 3 \otimes \bar{3} \otimes \bar{3} = 1 \oplus 1 \oplus 8 \oplus 8 \oplus 8 \oplus 8 \oplus 10 \oplus \overline{10} \oplus 27. \tag{11}$$

which yields two linearly independent color-singlet objects, as evidenced by the two-fold occurrence of the 1 irrep in Eq. (11). Let $p(x)$, $q(x)$, $r(x)$, $s(x)$ denote distinct fields which transform as color vectors in the fundamental 3 irrep, then $p^*(x)$, $q^*(x)$ transform according to the complex-conjugate $\bar{3}$ irrep. For distinct fields, there are $3^4 = 81$ basis operators formed by the color fields, $p^*_a(x)q^*_b(x)r_c(x)s_d(x)$. The following combinations are both linearly independent and gauge-invariant

$$T_S = (\delta_{ac}\delta_{bd} + \delta_{ad}\delta_{bc})p^*_a(x)q^*_b(x)r_c(x)s_d(x), \tag{12}$$

$$T_A = (\delta_{ac}\delta_{bd} - \delta_{ad}\delta_{bc})p^*_a(x)q^*_b(x)r_c(x)s_d(x), \tag{13}$$

and so they form a basis with which to construct our elemental tetraquark operators, fulfilling the need for *two* linearly independent color singlet operators from Eq. (11). Other color objects can be formed using, for example, link variables in different color irreps, but as long as only two quark and two antiquark fields are present, Clebsch-Gordan coefficients can be used to show that such objects are expressible in terms of the above operators, with possibly gauge-invariant gluon loops.

Each of the color-vector fields $p(x)$, $q(x)$, $r(x)$, $s(x)$ above can be one spin component of a local quark field, a smeared quark field, or an appropriately covariantly displaced and smeared quark field, but each must transform as a color three-vector at site x. Using a variety of different combinations of the Dirac indices and covariant displacements of the quark/antiquark fields allows us to construct a very large number of tetraquark operators having differing spin, orbital, and radial structures. We designed and implemented hundreds of tetraquark operators with different flavor, spin, and spatial constructions. The spatial configurations we use are shown in Fig. 1. We employ single-site operators (SS), doubly displaced operators in an I configuration (DDIa and DDIb), and quadruply displaced operators in a cross configuration (QDXa and QDXb). The letters "a" and "b" in the label denote different orderings of displacing the quarks and antiquarks. For each label, there are two color structures corresponding to Eqs. (12) and (13).

Each of our tetraquark operators which annihilates a state of three-momentum $\boldsymbol{p}$ is a linear superposition of gauge-invariant elemental operators

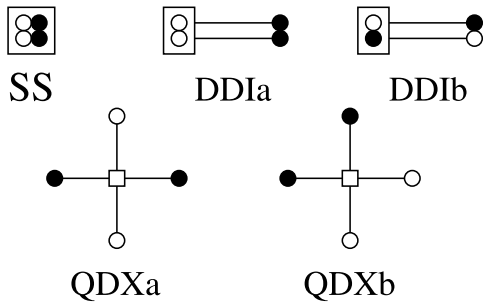


FIG. 1. Our tetraquark operators consist of two gauge-covariantly displaced quarks (open circles) and two displaced antiquarks (solid circles) arranged in the spatial configurations shown above. The boxes indicate locations where color and spin indices are connected. The different spatial configurations we use are single-site operators (SS), doubly displaced operators in an I configuration (DDIa and DDIb), and quadruply displaced operators in a cross configuration (QDXa and QDXb). The letters "a" and "b" in the labels denote the different orderings of displacing the quarks and antiquarks. For each label, there are two color structures, given by Eqs. (12) and (13).

$$\Phi^{ABCD\pm}_{\alpha\beta\mu\nu;ijkl}(t) = \sum_{\boldsymbol{x}} e^{-i\boldsymbol{p}\cdot\boldsymbol{x}}(\delta_{ab}\delta_{cd} \pm \delta_{ad}\delta_{bc})\bar{q}^{A}_{a\alpha i}(\boldsymbol{x},t) \times q^{B}_{b\beta j}(\boldsymbol{x},t)\bar{q}^{C}_{c\mu k}(\boldsymbol{x},t)q^{D}_{d\nu l}(\boldsymbol{x},t), \quad (14)$$

where $q, \bar{q}$ are defined in Eq. (4) of Ref. [23], A, B, C, D indicate flavor, and α, β, μ, ν are spin indices, i, j, k, l indicate quark-displacement types, and a, b, c, d are color indices. In this form, we do not need any additional phase factors to properly handle G-parity, as we do with the moving mesons. The "barred" operators which create a state of momentum $\boldsymbol{p}$ then take the form

$$\bar{\Phi}^{ABCD\pm}_{\alpha\beta\mu\nu;ijkl}(t) = \sum_{\boldsymbol{x}} e^{i\boldsymbol{p}\cdot\boldsymbol{x}}(\delta_{ab}\delta_{cd} \pm \delta_{ad}\delta_{bc})\bar{q}^{D}_{d\nu l}(\boldsymbol{x},t) \times q^{C}_{c\mu k}(\boldsymbol{x},t)\bar{q}^{B}_{b\beta j}(\boldsymbol{x},t)q^{A}_{a\alpha i}(\boldsymbol{x},t). \quad (15)$$

Each tetraquark sink operator has the form

$$T_{l\pm}(t) = c^{(l)}_{\alpha\beta\mu\nu;ijkl}\Phi^{ABCD\pm}_{\alpha\beta\mu\nu;ijkl}(t), \quad (16)$$

(or is a flavor combination of the above form), where l is a compound index comprised of a three-momentum $\boldsymbol{p}$, an irreducible representation Λ of the lattice symmetry group, the row λ of the irrep, total isospin I and isospin projection I_3, strangeness S, and an identifier labeling the different operators in each symmetry channel. Here, we focus on mesons containing only u, d, s quarks. The corresponding source operators are

$$\bar{T}_{l\pm}(t) = c^{(l)*}_{\alpha\beta\mu\nu;ijkl}\bar{\Phi}^{ABCD\pm}_{\alpha\beta\mu\nu;ijkl}(t). \quad (17)$$

Group-theoretical projections are carried out to determine the superposition coefficients $c^{(l)}_{\alpha\beta\mu\nu;ijkl}$ so that the resulting operators transform irreducibly under the little group of $\boldsymbol{p}$. These superposition coefficients are available upon request. The different flavor structures of our tetraquark annihilation operators are presented in Table II.

Although the color structures of our tetraquark operators make these operators seem very similar to our meson-meson operators, the individual color-contracted quark-antiquark pairs in a tetraquark are not each formed with a separate individual well-defined momentum nor does each pair transform irreducibly under any symmetry except color. Only the full combination of the two quark-antiquark pairs is formed with well defined momentum and spin/orbital transformation properties.

TABLE II. Flavor content of our isodoublet strange and isotriplet nonstrange tetraquark annihilation operators for isospin projection $I_3 = I$. Ordering of the quark/antiquark fields is the same as the annihilation operators shown in Eq. (14).

Isospin	Strangeness	Flavor content
$\frac{1}{2}$	1	$\bar{s}u\bar{s}s$
$\frac{1}{2}$	1	$\bar{s}u(\bar{u}u + \bar{d}d)$
$\frac{1}{2}$	1	$\bar{s}u(\bar{u}u - \bar{d}d) - \sqrt{2}\bar{s}d\bar{d}u$
1	0	$(\bar{u}u + \bar{d}d)\bar{d}u$
1	0	$\bar{s}s\bar{d}u$
1	0	$\bar{d}u(\bar{u}u - \bar{d}d) - (\bar{u}u - \bar{d}d)\bar{d}u$

D. Calculational details

This exploratory study was conducted using $N_{\rm cf} = 412$ gauge field configurations generated by the Hadron Spectrum collaboration [25,26] on an anisotropic lattice of size $32^3 \times 256$ with a spatial length $L = 3.74$ fm and a pion mass of approximately 230 MeV, using $N_f = 2 + 1$ Wilson clover-improved fermions. Ensemble details are given in Table III, and the action is described in Ref. [25].

The temporal correlators are evaluated using the Monte Carlo method as usual in lattice QCD. For the LapH smearing of the quark fields, the number of eigenvectors retained is $N_v = 264$, and the three-dimensional covariant Laplacian operator is constructed using stout-smeared spatial links with a staple weight of $\rho = 0.1$ and $N_\rho = 10$ iterations. Including multihadron operators in our correlation matrices requires the use of time slice to time slice quark propagators. To make the calculations of the temporal correlators feasible, we resort to employing stochastic estimates of such quark propagators. The stochastic LapH method [14] is used. For quark lines that connect the source and sink time slices, the noise dilution scheme (TF, SF, LI8) is utilized (see Ref. [14] for more details). This indicates full time dilution (TF), full spin dilution (SF), and interlace-8 for the LapH eigenvector dilution (LI8). For correlators which involve quark lines that originate and terminate at the final sink time, the dilution scheme (TI16, SF, LI8) was found to work well.

E. Operator selection

The quantum numbers associated with the $a_0(980)$ resonance are $I^G(J^{PC}) = 1^-(0^{++})$ and strangeness $S = 0$, so the first channel of interest in this lattice QCD study is the isotriplet, nonstrange, A^-_{1g} symmetry sector having total zero momentum. In this nomenclature, the subscript g indicates positive parity and the superscript, -, indicates

TABLE III. Details of the Monte Carlo ensemble used in this work and some stable meson masses. $N_{\rm cf}$ is the number of gauge-field configurations used. The temporal lattice spacing $a_t = 0.033357(59)$ fm is taken from Ref. [27]. Results from our determinations of the masses $m_\pi, m_K, m_\eta, m_{\eta'}$ of the pion, kaon, η, and η' mesons, respectively, are given in terms of a_t and are described later in Sec. III. The renormalized anisotropy $\xi = a_s/a_t = 3.451(11)$ is taken from Ref. [28], where a_s is the spatial lattice spacing. The lattice extent $(L/a_s)^3 \times (T/a_t)$ is $32^3 \times 256$.

$N_{\rm cf}$	$a_t m_\pi$	$a_t m_K$	$a_t m_\eta$	$a_t m_{\eta'}$
412	0.03953(17)	0.08348(14)	0.0979(30)	0.165(12)

TABLE IV. Single-meson operators used in the $a_0(980)$ and κ channels. These operators annihilate states of total zero momentum. The particle names refer to flavor content only, as described in Table I. The spatial and spin configuration of each operator is indicated by its superscript. The letters in the superscripts have been described in Sec. II B, and the final number is an index that differentiates the different operators of the same spatial configuration.

$A_{1g}^-, I=1, S=0$	$A_{1g}, I=\frac{1}{2}, S=1$
$\pi^{SD2}_{A_{1g}^-}$	$K^{DDL2}_{A_{1g}}$
$\pi^{TDO3}_{A_{1g}^-}$	$K^{TDO3}_{A_{1g}}$
	$K^{TDU5}_{A_{1g}}$

negative G-parity. The quantum numbers associated with the κ resonance are $I(J^P)=\frac{1}{2}(0^+)$ and strangeness $S=1$, so the second channel of interest in our lattice QCD study is the isodoublet, strangeness 1, A_{1g} symmetry sector with total zero momentum. To probe these two resonances, we need to include operators capable of creating all of the stationary states in finite volume whose energies lie below $E_{\max}$, where $E_{\max}$ should lie somewhat above the expected energies of these resonances. We decided to choose $E_{\max}\sim 3m_K$, where m_K is the mass of the kaon.

First, we choose a handful of single-meson operators in order to capture any states that are predominantly quark-antiquark states. The single-meson operators we selected in the two channels are listed in Table IV. More will be said about these single-meson operators below. From prior computations, the energies of a single pion, kaon, η and ϕ having particular momenta have been determined, so the noninteracting energies of any two of these particles are known. We determine all of the two particle combinations that produce noninteracting energies below $E_{\max}$ in these channels, then include the two-meson operators expected to create these states. The two-meson operators we selected in the two channels are listed in Table V. The lowest noninteracting energy of three mesons in each channel lies above $E_{\max}$, so no three-meson operators are needed. The four-meson thresholds in the κ and $a_0(980)$ channels occur near $2.4m_K$ and $2.6m_K$, respectively. Since incorporating four-meson operators into this exploratory study would be very costly, we did not include them. In so doing, our results above these thresholds must be considered with caution. Since the effects of the tetraquark operators occur well below the four-meson thresholds, the main conclusions of this work are not affected by this decision to exclude four-meson operators.

In Tables IV and V, the spatial and spin configuration of each single-meson operator is indicated by its superscript. The letters in the superscripts have been previously described in Sec. II B, and the final integer in each superscript is an index that differentiates the different single-meson operators of the same spatial/spin configuration. The complete details of our single-meson and two-meson operators are available upon request.

TABLE V. Two-meson operators used in the $a_0(980)$ and κ channels. These operators annihilate states of total zero momentum. The particle names refer to flavor content only, as described in Table I. The spatial and spin configuration of each operator is indicated by its superscript. The letters in the superscripts have been described in Sec. II B, and the final number is an index that differentiates the different operators of the same spatial configuration. The number in parentheses following a particle name denotes $\boldsymbol{n_p}^2$, related to the square of its total momentum by $\boldsymbol{p}^2=(2\pi/L)^2\boldsymbol{n_p}^2$ for spatial volume L^3, and the subscript denotes its little group irrep.

$A_{1g}^-, I=1, S=0$	$A_{1g}, I=\frac{1}{2}, S=1$
$K(0)^{SS0}_{A_{1u}}\bar{K}(0)^{SS0}_{A_{1u}}$	$K(0)^{SS0}_{A_{1u}}\pi(0)^{SS0}_{A_{1u}^-}$
$K(1)^{SS1}_{A_2}\bar{K}(1)^{SS1}_{A_2}$	$K(0)^{SS0}_{A_{1u}}\tilde{\eta}(0)^{SS0}_{A_{1u}^+}$
$K(2)^{SS0}_{A_2}\bar{K}(2)^{SS0}_{A_2}$	$K(0)^{SS0}_{A_{1u}}\tilde{\phi}(0)^{SS0}_{A_{1u}^+}$
$K(2)^{SS1}_{A_2}\bar{K}(2)^{SS1}_{A_2}$	$K(1)^{SS1}_{A_2}\pi(1)^{SS1}_{A_2^-}$
$\tilde{\eta}(0)^{SS0}_{A_{1u}^+}\pi(0)^{SS0}_{A_{1u}^-}$	$K(1)^{SS1}_{A_2}\tilde{\eta}(1)^{SS1}_{A_2^+}$
$\tilde{\eta}(1)^{SS0}_{A_2^+}\pi(1)^{SS0}_{A_2^-}$	$K(1)^{SS1}_{A_2}\tilde{\phi}(1)^{SS1}_{A_2^+}$
$\tilde{\eta}(2)^{SS1}_{A_2^+}\pi(2)^{SS1}_{A_2^-}$	$K(2)^{SS0}_{A_2}\pi(2)^{SS0}_{A_2^-}$
$\tilde{\phi}(0)^{SS0}_{A_{1u}^+}\pi(0)^{SS0}_{A_{1u}^-}$	$K(3)^{SS0}_{A_2}\pi(3)^{SS0}_{A_2^-}$
$\tilde{\phi}(1)^{SS1}_{A_2^+}\pi(1)^{SS1}_{A_2^-}$	
$\tilde{\phi}(2)^{SS0}_{A_2^+}\pi(2)^{SS0}_{A_2^-}$	

The single-meson operators listed in Table IV are selected based on a low-statistics Monte Carlo computation. In each symmetry channel, the correlation matrix for a fairly large number of single-meson operators is evaluated and the analysis procedure described in Sec. II A is applied to obtain the $|Z_j^{(n)}|$ overlap factor magnitudes for all of the operators. From this correlation matrix, a half dozen or so operators which produce a state with the largest overlaps onto the ground state in each channel are identified and retained. The correlation matrix of the retained single-meson operators and all of the two-meson operators in Table V in each symmetry channel is then evaluated and examined. In each symmetry channel, some of the single-meson operators lead to an ill-conditioned correlator matrix, suggesting a lack of linear independence, or introduce an excessive amount of statistical noise. These operators are removed to produce our final operator set. The remaining single-meson operators are those listed in Table IV. In the $a_0(980)$ channel, we are left with a singly displaced (SD) and a triply displaced orthogonal (TDO) operator, and in the κ channel, a doubly displaced-L (DDL), triply displaced-orthogonal (TDO), and a triply displaced-U (TDU) operator survive the selection process.

With these reduced operator sets (Tables IV and V), good quality fits to the diagonal elements of the rotated correlators are obtained in each channel following the procedure

described in Sec. II A. The important question we address in this work is: have any energy levels been missed which are important for revealing the $a_0(980)$ and κ resonances?

To obtain information about the $a_0(980)$ and κ resonances in lattice QCD, the elements of the infinite-volume scattering K matrix must first be parametrized, then the best-fit values of the parameters are obtained using a well-known quantization condition [15–18] involving the finite-volume spectrum of states obtained in lattice QCD. The masses and widths of the resonances follow from the details of the K matrix. To apply this so-called Lüscher method reliably, the energies of *all* of the finite-volume eigenstates with some overlap onto the two-particle scattered states are required in the energy range near the energy of the resonance. If an energy is missed, the quantization condition could lead to an incorrect determination of the K matrix.

Although tetraquark operators are similar to two-meson operators, they are different enough that the possibility exists of missing an eigenstate by not including them. To test this, we designed hundreds of tetraquark operators as described in Sec. II C with differing flavor structures, color structures, and displacements. Of course, it is not feasible to include hundreds of operators all at once in a correlation matrix. Our approach for selecting the best few tetraquark operators to include proceeds as follows.

First, the diagonal correlators for each of the hundreds of tetraquark operators are evaluated in an initial low-statistics computation on 25 gauge configurations. The effective energies corresponding to most of these diagonal correlators show very large statistical errors and/or are very high-lying. The tetraquark operators associated with these very noisy and/or high-lying effective energies are discarded from consideration, leaving 60 operators in the κ channel, and 32 in the $a_0(980)$ channel.

Next, we add, one by one, each of the remaining tetraquark operators to the basis of single-meson and two-meson operators listed in Tables IV and V, evaluate the correlation matrix in each channel using 25 gauge configurations, apply the analysis procedure described in Sec. II A using $\tau_N = 3, \tau_0 = 4, \tau_D = 7$, and carry out appropriate fits to the diagonal elements of the rotated correlator matrix $\tilde{C}(t)$ of Eq. (4). For the majority of the tetraquark operators, the spectrum determinations of low-lying states obtained by this procedure do not change significantly. However, for a few similarly structured tetraquark operators in each symmetry channel, some substantial changes in the low-lying energy extractions are observed.

In the κ channel, the third and fourth lowest-lying energy extractions are substantially lowered for a few operators, while in the $a_0(980)$ channel, a lowering of the lowest and third lowest-lying energies is seen for a few operators, with some movements of other energies. In the $a_0(980)$ channel, we find that only tetraquark operators with the $(\bar{u}u + \bar{d}d)\bar{d}u$ flavor structure yield a significant change in the spectrum extraction of the low-lying finite-volume states, while in the κ channel, we find that only tetraquark operators with the $\bar{s}u\bar{s}s$ flavor structure yield substantial modifications of the energy determinations. The operators that produce the substantial changes in each channel include both color structures and a variety of spatial configurations. In each symmetry channel, the operator yielding either the largest lowering of energy extractions or the effective energy with the smallest statistical errors and/or least amount of excited-state contamination is identified and selected as the best tetraquark operator to utilize. The chosen best tetraquark operator in each symmetry channel is listed in Table VI. A color symmetric operator was chosen in the $a_0(980)$ sector, while a color antisymmetric operator was selected in the κ channel. Further details about these operators, such as the exact definition of the single-site operator designated by an SS2 superscript, are available from the authors upon request. Note that the choice of the so-called best operator is not likely to be crucial, as long as one of the few operators producing the substantial changes is employed. Further details about our tetraquark operator selection procedure are presented in the Supplemental Material [29].

TABLE VI. The tetraquark operators selected in the $a_0(980)$ and κ channels. These operators annihilate states of total zero momentum and are both single-site opeators, as indicated by the superscripts. The final number in the superscript is an index that differentiates the different operators of the same spatial configuration, and the $\pm$ in parentheses indicates the color structure.

$A_{1g}^-, I = 1, S = 0$	$A_{1g}, I = \frac{1}{2}, S = 1$
$T[(\bar{u}u + \bar{d}d)\bar{d}u]_{A_{1g}^-}^{SS2(+)}$	$T[\bar{s}u\bar{s}s]_{A_{1g}}^{SS2(-)}$

This procedure is then repeated. Each of the 59 κ-channel and 31 $a_0(980)$-channel tetraquark operators that are not selected in the first step above are individually, one by one, added to the basis of operators listed in Tables IV, V, and VI, the correlation matrix in each channel is evaluated using 25 gauge configurations, the analysis procedure described in Sec. II A is again applied, and appropriate fits to the diagonal elements of the rotated correlator matrix $\tilde{C}(t)$ of Eq. (4) are carried out to see if any further changes occur to the low-lying spectra. In this second step, no new substantial changes to any of the low-lying energy extractions are found. For this reason, no additional tetraquark operators are included in our basis of interpolating operators.

Two-meson operators having larger relative momenta are also included in a low-statistics run to see if such operators could have any effect on the low-lying spectrum determination, and no such effect is observed. Given this, we use the operators described in Tables IV, V, and VI for the higher-statistics computations.

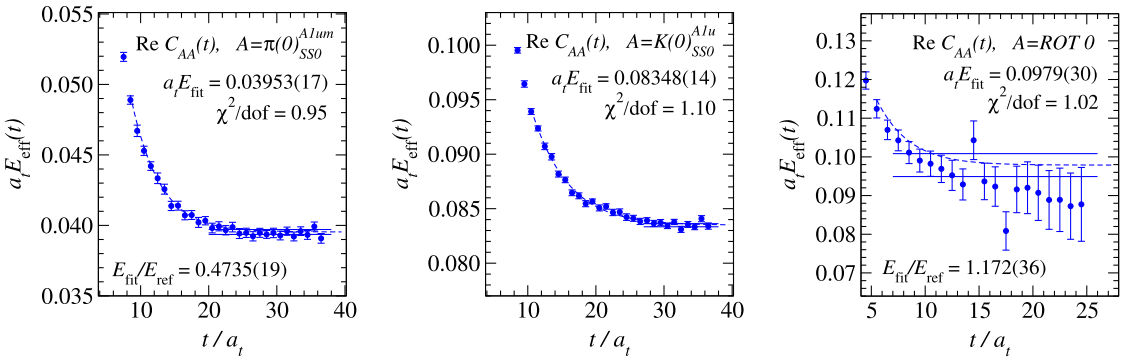


FIG. 2. Effective energies for the at-rest pion (left), kaon (center), and η meson (right). The symbols with error bars indicate the Monte Carlo estimates of the effective energy functions, and fitting information is provided by the dashed and solid blue curves, which are explained in the text. Fit results for the dimensionless products of the temporal lattice spacing a_t times the meson masses are shown, along with fit quality $\chi^2/N_{\rm dof}$. Fits to the correlators are done using a sum of two exponentials as the fit model. The vertical displacements of the effective energy points for the η meson at time separations 14.5 a_t and 17.5 a_t is caused by using an interlace-16 time dilution scheme for the disconnected contributions. Energies were also obtained for these mesons at a variety of different momenta. The operators used to obtain the single-meson masses are discussed in the text in Sec. III A. The reference energy $E_{\rm ref}$ is taken to be the mass of the kaon.

III. FINITE-VOLUME SPECTRA

Our results for the lowest-lying energies of the stationary states in finite volume are presented and discussed in this section, with details of how our results are obtained. Energies are determined both as dimensionless products with the temporal lattice spacing a_t and as dimensionless ratios over a reference energy $E_{\rm ref}$, which we take to be the kaon mass $E_{\rm ref} = m_K$. After discussing the determinations of the single-meson masses and energies in Sec. III A, results for the κ channel are presented first in Sec. III B since statistical errors are smaller in this channel, then results for the $a_0(980)$ channel are discussed in Sec. III C.

Below, so-called effective energy plots are used to illustrate some of our fits. For a given diagonal element $\tilde{C}_{jj}(t)$ of a pivoted correlator matrix, the effective energy is defined by

$$a_t E^{(j)}_{\rm eff}(t) = \frac{1}{\Delta}\ln\left(\frac{\tilde{C}_{jj}(t-\frac{1}{2}\Delta)}{\tilde{C}_{jj}(t+\frac{1}{2}\Delta)}\right), \tag{18}$$

where $\Delta = 3a_t$ is used throughout this work, and the time separation $t = \frac{5}{2}a_t, \frac{7}{2}a_t, \frac{9}{2}a_t, \ldots$ takes half-integral multiples of the temporal lattice spacing a_t. The operator whose temporal correlations give $\tilde{C}_{jj}(t)$ typically creates many states when acting on the vacuum. Denote $E^{(j)}_{\rm lowest}$ as the lowest-lying energy of the states produced by this operator, then as t becomes large, the effective energy tends toward $E^{(j)}_{\rm lowest}$. Contributions from higher lying states are usually visible for small values of t.

In Fig. 2, as well as in all other effective energy plots shown later in this work, the symbols with error bars indicate Monte Carlo estimates of the effective energy function given by Eq. (18) associated with pivoted temporal correlator $\tilde{C}_{jj}(t)$. To extract energies, fits to these correlators using a model which is either a single exponential or a sum of two exponentials are carried out. The effective energy reconstructed from the best fit is shown as a dashed blue line in each effective energy plot, and this line is shown only in the time separation range used in the fit. Two horizontal solid blue lines indicate the statistical uncertainty in the best fit value of the energy in each plot.

A. Single-meson energies

Electromagnetic and weak nuclear effects are ignored in our study, and the masses of the u and d quarks are taken to be the same so that isospin is a good symmetry. With these approximations, only decays by the strong force are permitted. The pion and kaon are stable since they are the lightest nonstrange and strange mesons. Since the mass of the η here is less than the energy of three pions at rest, the η is a stable meson. The dominant decay mode of the η' meson is $\pi\pi\eta$, while its decay to three pions is dramatically suppressed. Given the suppression of the decay mode to three pions and the fact that the η' mass here is less than sum of the masses of $\pi\pi\eta$, the η' can approximated as stable.

Our results for the masses of these stable mesons are listed in Table III. Our determinations of the pion, kaon, and η masses are illustrated in the effective energy plots shown in Fig. 2. The pion and kaon energies are obtained using single correlators involving only the simplest single-site pion and kaon operators, respectively. Since our $\tilde{\eta}$ and $\tilde{\phi}$ operators actually have $\bar{u}u + \bar{d}d$ and $\bar{s}s$ flavor structure, the η and η' energies are obtained using variationally improved single-hadron operators, which are linear combinations of the single-hadron operators determined by solving a GEVP in the subspace created by the single-hadron $\tilde{\eta}$ and $\tilde{\phi}$ operators. For each momentum, two "rotated" single-hadron operators

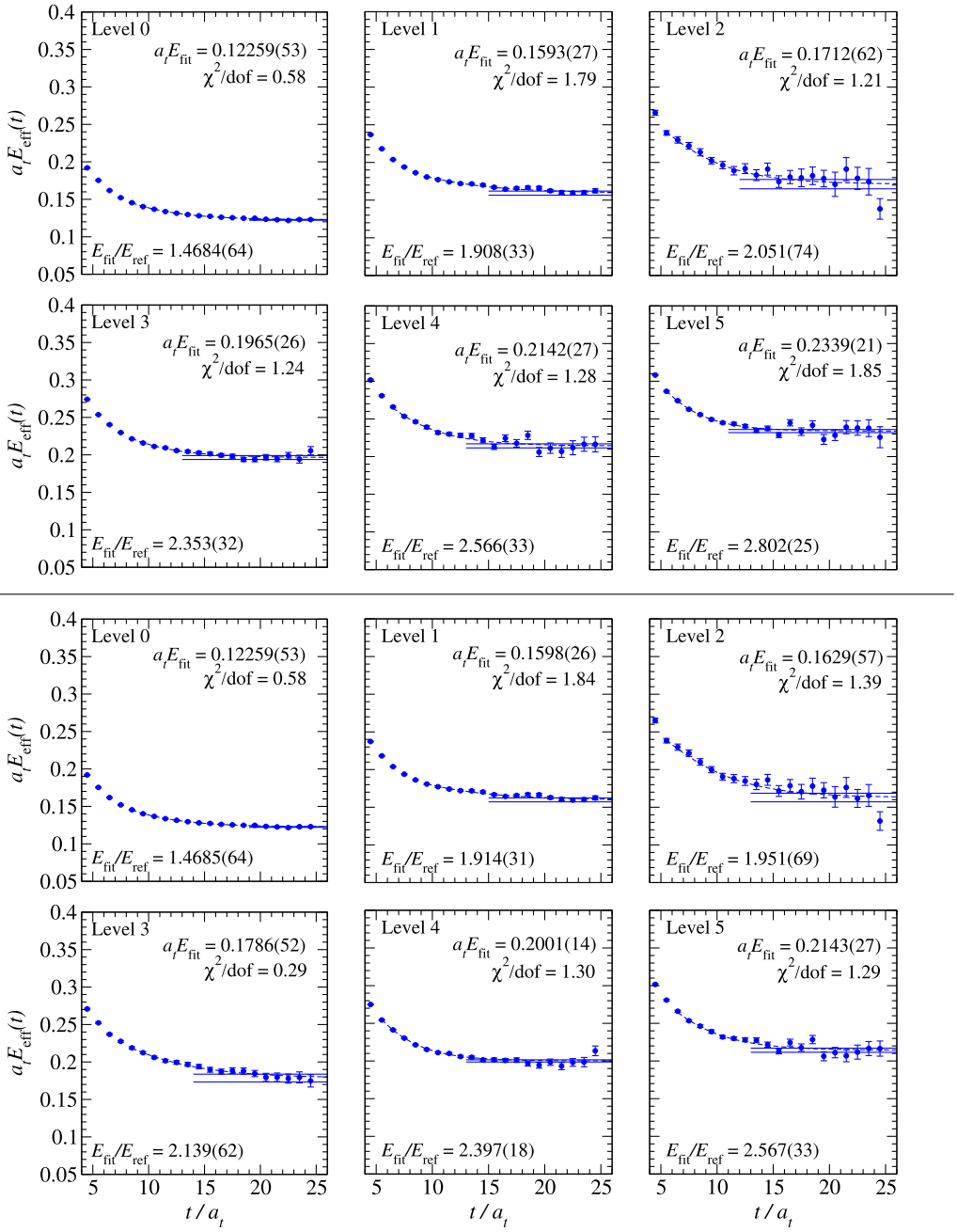


FIG. 3. Effective energies for the lowest six levels in the isodoublet, strangeness 1, zero-momentum, A_{1g} channel. Top two rows: results obtained using only the operators in Tables IV and V, excluding the tetraquark operator. Bottom two rows: results obtained using the operators in Tables IV and V and also including the tetraquark operator in Table VI. Effective energy curves calculated from correlator fits are overlaid, and fit results are shown. Note that level 3 in the bottom row corresponds to the additional level found using the tetraquark operator.

are obtained in this way and are denoted here by ROT 0 and ROT 1. The operators named ROT 0 are used to obtain the η energies, and the ROT 1 operators are used to determine the η' energies.

B. Channel involving the κ resonance

Results for the stationary-state energies in the isodoublet, strangeness 1, zero-momentum A_{1g} channel are presented in this section. The results shown are obtained using a normalization time, metric time, and diagonalization time in the GEVP given by $\tau_N = 3$, $\tau_0 = 6$, and $\tau_D = 12$, respectively.

Fits to the diagonal elements of the correlator matrix $\tilde{C}(t)$, obtained after the single-pivot procedure described in Sec. II A, are shown as effective energy plots in Fig. 3. In the top two rows are shown the fits which yield the lowest

TABLE VII. Fit details for estimating the energies in the isodoublet strange zero-momentum A_{1g} channel using the operator basis excluding the tetraquark operator. Energies E are listed in terms of the temporal lattice spacing a_t and as ratios over the reference energy $E_{\text{ref}} = m_K$. Fits are done using either a two-exponential model (2-exp) or a single-exponential model (1-exp) to the diagonal elements of the $\tilde{C}(t)$ correlator matrix for times $t = t_{\text{min}}, \ldots, t_{\text{max}}$. Note that $\tau_{\text{min}} = t_{\text{min}}/a_t$ and $\tau_{\text{max}} = t_{\text{max}}/a_t$. The rightmost column gives the chi-square per degree of freedom of each best fit.

E/E_{ref}	a_tE	Fit model	$(\tau_{\text{min}}, \tau_{\text{max}})$	χ^2/N_{dof}
1.4684(64)	0.12259(53)	2-exp	(7, 26)	0.58
1.908(33)	0.1593(27)	2-exp	(8, 26)	1.79
2.051(74)	0.1712(62)	2-exp	(4, 26)	1.21
2.353(32)	0.1965(26)	2-exp	(7, 26)	1.24
2.566(33)	0.2142(27)	2-exp	(5, 26)	1.28
2.802(25)	0.2339(21)	2-exp	(4, 26)	1.85
2.924(92)	0.2441(76)	1-exp	(11, 26)	1.11
2.95(18)	0.246(15)	1-exp	(9, 19)	0.97
3.289(96)	0.2746(81)	2-exp	(3, 26)	1.49

six energies using only the single-meson and meson-meson operators (eleven in total) listed in Tables IV and V, excluding the tetraquark operator. In the bottom two rows are presented the fits which yield the lowest six energies using all twelve operators listed in Tables IV and V and also including the tetraquark operator in Table VI. Only the fits for the six lowest-lying energies are shown, but higher energies were also obtained. Fit details are given in Tables VII and VIII. Fits using a sum of two exponentials are mainly utilized, but for a few of the higher-lying energies, the excited-state contamination at early times is not sufficiently precise enough to allow the parameters of the second exponential to be reliably determined, and so fits using only a single exponential are employed in these few cases. In each fit, only the correlator values for time separations in the range $t_{\text{min}} \leq t \leq t_{\text{max}}$ are used. t_{max} is chosen to be the earliest time at which the correlator value becomes statistically consistent with zero. t_{min} is taken to be the earliest time at which the fit quality is reasonably good and the best fit value of the energy is consistent with values obtained using larger values of starting time. Note that the fit qualities in Tables VII and VIII are all reasonably good. The results obtained with only the meson and meson-meson operators do not themselves give any hint of a missing energy level.

Our procedure for selecting the GEVP parameters τ_N, τ_0, and τ_D is as follows. τ_N simply needs to be small. The metric time τ_0 is generally chosen to be approximately $\tau_D/2$. In practice, we find results for the energies are very insensitive to this parameter as long as it is not very small nor very large. The diagonalization time τ_D is the most important to choose well. If too small a value is used, the diagonalization may be contaminated by higher lying states and the $\tilde{C}(t)$ correlator matrix does not remain diagonal within statistical errors for $t > t_D$, noting that $t_D = \tau_D a_t$. If too large a value is used, the diagonalization may be contaminated by statistical noise, leading to larger uncertainties. Our procedure is to vary τ_D to find the intermediate window where errors are not overly large, all off-diagonal elements of $\tilde{C}(t)$ remain zero within statistical errors for all $t > t_D$ that have reasonable uncertainties, and the energy extractions are insensitive to the choice of τ_D. We found that choosing $\tau_D = 12$ yielded a good combination of reduced noise and a sufficiently diagonal matrix $\tilde{C}(t)$ for $t > t_D$. To ensure our results were insensitive to our choice of GEVP parameters within the window, the spectrum was extracted for various choices and compared. A comparison of the spectra for three choices of τ_D is shown in Fig. 4.

TABLE VIII. Fit details for estimating the energies in the isodoublet strange zero-momentum A_{1g} channel using the operator basis that includes the tetraquark operator. See the caption of Table VII for further information about notation and headings.

E/E_{ref}	a_tE	Fit model	$(\tau_{\text{min}}, \tau_{\text{max}})$	χ^2/N_{dof}
1.4685(64)	0.12259(53)	2-exp	(7, 26)	0.58
1.914(31)	0.1598(26)	2-exp	(8, 26)	1.84
1.951(69)	0.1629(57)	2-exp	(4, 26)	1.39
2.139(62)	0.1786(52)	2-exp	(7, 26)	0.29
2.397(18)	0.2001(14)	2-exp	(4, 26)	1.3
2.567(33)	0.2143(27)	2-exp	(5, 26)	1.29
2.79(15)	0.233(13)	1-exp	(11,26)	1.37
2.797(24)	0.2335(20)	2-exp	(4, 26)	1.71
2.82(16)	0.235(13)	1-exp	(11, 26)	1.04
3.291(95)	0.2748(80)	2-exp	(3, 26)	1.5

In order to obtain some information about the structures of the stationary states, the overlap factors $|Z_j^{(n)}|^2$ are

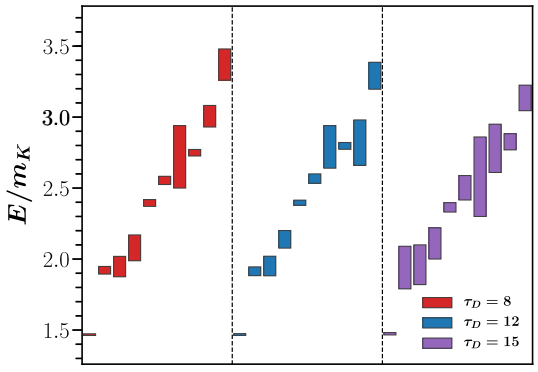


FIG. 4. Determinations of the spectrum in the isodoublet strange zero-momentum A_{1g} channel obtained using three different diagonalization times $\tau_D = 8$ (left), $\tau_D = 12$ (center), and $\tau_D = 15$ (right) for the operator basis given in Tables IV, V, and VI, which includes the tetraquark operator. The metric times τ_0 are chosen as $\tau_D/2$, rounded up. Good agreement is found, but a significant increase in statistical uncertainties is evident for $\tau_D = 15$.

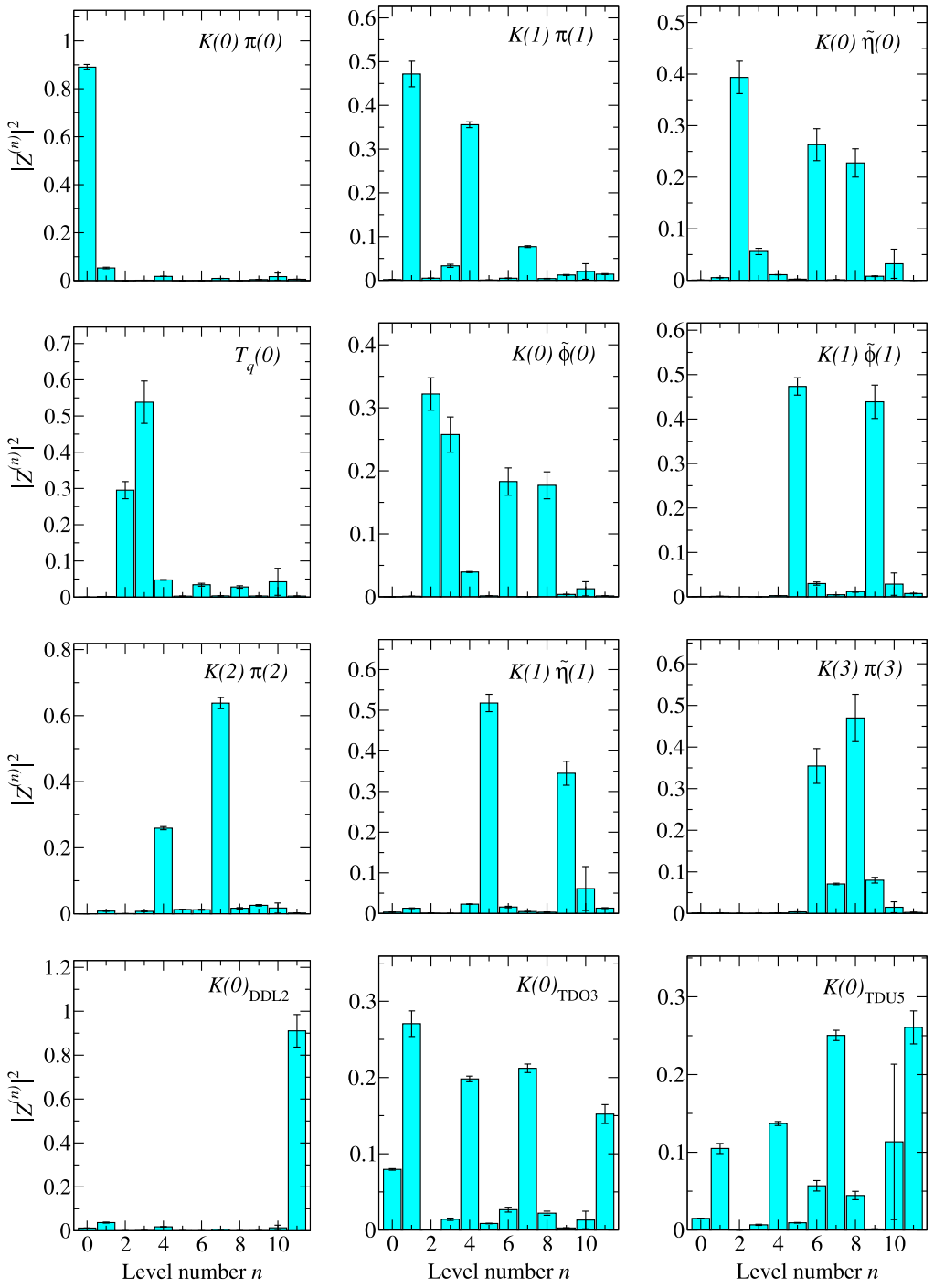


FIG. 5. Overlap factors $|Z_j^{(n)}|^2$ for the twelve operators used in the correlator matrix corresponding to the isodoublet strange zero-momentum A_{1g} channel. Each plot shows the factors for a single operator, with horizontal axis labeled by n, the index identifying the stationary states. The factors for the tetraquark operator are shown in the left-most plot in the second row from the top. Levels 3 and 2 have significant tetraquark, $K\tilde{\eta}$, and $K\tilde{\phi}$ content, where $\tilde{\eta}$ means $\bar{u}u + \bar{d}d$ and $\tilde{\phi}$ means $\bar{s}s$.

determined for all twelve operators and are shown in Fig. 5. Each plot shows the factors for a single operator, with horizontal axis labeled by n, the index identifying the stationary states. Within each plot, the heights have been rescaled so that they add to unity, but keep in mind that overlaps with levels for $n \geq 12$ have not been determined.

First, consider the lowest-lying level 0. An inspection of the overlap plots in Fig. 5 shows that this state is predominantly created by the $K(0)\pi(0)$ operator. Hence, level 0 can be viewed as a state dominated by a pion at rest and a kaon at rest with residual interactions. Next, consider stationary state level 1. Operators $K(1)\pi(1)$, $K(0)_{\mathrm{TDO3}}$, and

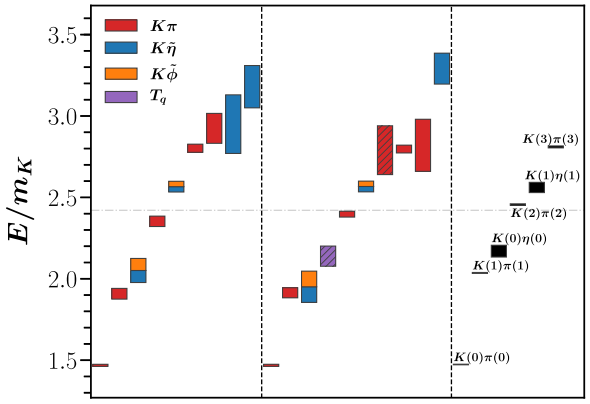


FIG. 6. Left: estimate of isodoublet, strangeness 1, zero-momentum, A_{1g} spectrum using operators in Tables IV and V, excluding the tetraquark operator. Center: estimate of the spectrum obtained using operators in Tables IV, V, and VI, which includes the tetraquark operator. Right: two-particle noninteracting energies. Statistical errors of the energy determinations are shown by the vertical extents of the boxes. The horizontal gray line indicates the four-particle $K\pi\pi\pi$ threshold (there are no three-particle states in this channel in this energy range). The four flavor contents of the twelve basis operators are indicated by colors as shown in the legend. Levels predominantly created by a single operator are indicated by a single color corresponding to the flavor of the operator. Dual colored levels are predominantly created by two of the basis operators with comparable overlap factors. Levels created mostly by a single operator but with significant overlaps from one or more other operators are indicated by a hatched box.

$K(0)_{\mathrm{TDU5}}$ produce states with non-negligible overlaps with this level, with $K(1)\pi(1)$ producing the largest overlap factor. Hence, level 1 can be viewed as mainly a $K\pi$ with back-to-back minimal nonzero momenta and residual interactions. The $K(0)\tilde{\eta}(0)$, $K(0)\tilde{\phi}(0)$, and the tetraquark $T_q(0)$ operators create states with significant overlap onto level 2, and the $K(0)\tilde{\phi}(0)$ and $T_q(0)$ operators create states with significant overlaps onto level 3. Since the state created by the tetraquark operator overlaps mainly with level 3, we qualitatively identify level 2 as a mixed $K\tilde{\eta} - K\tilde{\phi}$ state (shown as an orange and blue box) and level 3 predominantly as a tetraquark state with significant $K\tilde{\phi}$ mixing (shown as a hatched purple box). Again, keep in mind that for our operators, $\tilde{\eta}$ means $\bar{u}u + \bar{d}d$ and $\tilde{\phi}$ means $\bar{s}s$.

A summary of the spectrum is shown in the center panel of Fig. 6. The ten lowest-lying energy estimates are indicated by the colored boxes, horizontally displaced for improved visibility. Statistical errors of the energy determinations are shown by the vertical extents of the boxes. Using the overlap factors of Fig. 5 as described above, the predominant content of each level is determined and is indicated in Fig. 6 by the color of each energy estimate. The four flavor contents of the twelve basis operators are indicated by colors as shown in the legend. Levels predominantly created by a single operator are indicated by a single color corresponding to the flavor of the operator. Dual colored levels are predominantly created by two of the basis operators with comparable overlap factors. Levels created mostly by a single operator but with significant overlaps from one or more other operators are indicated by a hatched box. The horizontal gray line indicates the four-particle $K\pi\pi\pi$ threshold (there are no three-particle states in this channel in this energy range).

The six lowest-lying two-particle noninteracting energies are shown in the right panel of Fig. 6. For the noninteracting energies, η and ϕ refer to the physical particles, in contrast to our operator nomenclature. The lowest-lying level in the center panel corresponds to the $K(0)\pi(0)$ noninteracting state with a small energy shift. Level 4 corresponds with the $K(2)\pi(2)$ noninteracting level with a small shift, and level 5 appears to be associated with the $K(1)\eta(1)$ noninteracting level. The most substantial difference between the center and right panels is in the energy range between $(1.8 - 2.3)m_K$. In this energy range, there are only two noninteracting levels $K(1)\pi(1)$ and $K(0)\eta(0)$, whereas three levels are observed in the center panel in the presence of interactions, and the tetraquark operator clearly plays an important role in the emergence of this additional level.

An estimate of the spectrum obtained using an operator set that excludes the tetraquark operator is shown in the left panel in Fig. 6. In comparing this spectrum with that shown in the center panel, one sees that there is no change to the lowest-lying energy, and the levels at 2.35 m_K and 2.6 m_K are changed very little. In the left panel, the orange and blue box (level 2) near 2.05 m_K becomes two distinct energies in the center panel (levels 2 and 3). The energy of level 3 (the hatched purple box) in the center panel is slightly above the energy of level 2 in the left panel. Level 2 in the center panel, indicated by the orange and blue box, has an energy slightly below that of level 2 in the left panel.

This is the expected signature of a missed level in a lattice QCD correlator matrix analysis. In the left panel, there is only one operator, a linear superposition of the $K(0)\tilde{\eta}(0)$ and $K(0)\tilde{\phi}(0)$ operators, with significant overlap onto the true levels 2 and 3, as shown in the center panel. With only one such operator, the two distinct energies cannot be resolved, and a decay rate of the correlator is extracted that lies between these two energies. In the center panel, the addition of the tetraquark operator yields two operators which produce states with significant overlaps onto levels 2 and 3, and so, the two individual energies can be resolved.

Level 4 at an energy around 2.4 m_K in the center panel, shown as a red box, can be compared to level 3 in the left panel. The energy of level 3 in the left panel is slightly below that of the energy of level 4 in the center panel,

which is consistent with the signature of a missed level below these energies. The operator which mainly produces level 3 in the left panel creates a state which has a small overlap onto the two lower-lying states which are levels 2 and 3 in the center panel. This small overlap occurs because the state produced by the tetraquark operator is needed to fully remove this overlap and it is not available. This small leakage to lower-lying states leads to an energy extraction which is very slightly too low. Although this leakage causes this very slight downward shift in the estimate of the energy, its effect is too small to spoil an observed plateau in the effective energy.

Levels 0, 1, and 4 in the center panel (red boxes) of Fig. 6 are predominantly $K\pi$ states. The overlap factors in Fig. 5 associated with the tetraquark operator are essentially zero for levels 0 and 1, and very small for level 4. The tetraquark operator is observed to impact levels 2 and 3 mostly. An inspection of the overlap factors in Fig. 5 shows that $K\pi$ operators produce states with very little overlaps on levels 2 and 3. These facts indicate that the tetraquark operator is having an effect mainly in the $K\eta$ decay channel and not in the $K\pi$ channel.

We conclude that the tetraquark operator is very important for obtaining a reliable estimate of the finite-volume spectrum in this channel for energies below $2.7\ m_K$. Without the tetraquark operator, one level is missed that could be important in a study of resonances involving the $K\eta$ decay channel. The κ or $K_0^*(700)$ resonance decays mainly to $K\pi$, so it is not clear if missing the level created by the tetraquark operator would adversely affect a study of the κ resonance. However, the $K_0^*(1430)$ decays to both $K\pi$ and $K\eta$, so a missed low-lying state in the $K\eta$ channel could adversely impact a study of this resonance.

Above an energy of $2.7\ m_K$, statistical uncertainties in the energy extractions are very large, making comparisons between the left and center panels difficult. Fortunately, these levels are not relevant for an analysis of the κ resonance.

It is interesting to observe that our results shown in the left panel of Fig. 6, determined excluding the tetraquark operator, qualitatively agree with the results shown in Fig. 5 of Ref. [30] obtained also without any tetraquark operators, once adjustments for the different allowed momenta magnitudes are taken into account. The results in that work were obtained using ensembles with the same lattice action but with $m_\pi \approx 400$ MeV and small spatial extents of 16, 20, and 24, as compared to 32 in this work. The overlap factors in Fig. 5 of Ref. [30] show significant mixings between the $K\pi$ and single quark-antiquark operators. In the absence of the tetraquark operator, our overlap factors show a similar pattern, but this tendency disappears when the tetraquark operator is included. Without the tetraquark operator, the energy determinations become plagued by false plateaux, unfortunately leading to incorrect determinations of the overlap factors. It is also interesting to note that the three red $K\pi$ energies in the left panel of Fig. 6 are in reasonable agreement with results shown in the upper right plot of Fig. 4 in Ref. [31]. Our $K\pi$ levels agree with those shown (the two lowest) in Fig. 4 of Ref. [27], which used the same ensemble.

C. Channel involving the $a_0(980)$ resonance

Results for the stationary-state energies in the isotriplet nonstrange zero-momentum A_{1g}^- channel are presented in this section. The results shown are obtained using a normalization time, metric time, and diagonalization time of $\tau_N = 3$, $\tau_0 = 4$, and $\tau_D = 7$, respectively. The same procedure as described in Sec. III B is used to arrive at these choices for the GEVP parameters which yield a good combination of reduced noise and a sufficiently diagonal matrix $\tilde{C}(t)$ for $t > t_D$. To ensure our results were insensitive to our choice of GEVP parameters within the window, the spectrum was extracted for various choices and compared. The so-called disconnected contributions associated with the $\tilde{\eta}$ operators in this channel lead to significantly larger statistical errors in the determination of the correlation matrix, compared to the κ channel. This is the main reason that we end up using $\tau_D = 7$, which is substantially smaller than the value of 12 used in the κ channel.

Fits to the diagonal elements of the correlator matrix $\tilde{C}(t)$, obtained after the single-pivot procedure described in Sec. II A, are shown as effective energy plots in Fig. 7. In the top two rows are shown the fits which yield the lowest six energies using only the single-meson and meson-meson operators (twelve in total) listed in Tables IV and V, excluding the tetraquark operator. In the bottom two rows are presented the fits which yield the lowest six energies using all thirteen operators listed in Tables IV and V and also including the tetraquark operator in Table VI. Only the fits for the six lowest-lying energies are shown, but higher energies were also obtained. Fit details are given in Tables IX and X. As in the κ channel, note that the fit qualities in Tables IX and X are all reasonably good. The results obtained with only the meson and meson-meson operators do not themselves give any hint of unreliable energy extractions.

In order to obtain some information about the structures of the stationary states, the overlap factors $|Z_j^{(n)}|^2$ are computed. In this channel, the possibility exists that two states are present which are predominantly of quark-antiquark content, corresponding to the $a_0(980)$ and the $a_0(1450)$ mesons. We do not expect a one-to-one correspondence between these two quark-antiquark states and the two single-hadron operators in Table IV. Instead, a better one-to-one correspondence can be achieved using so-called variationally improved single-hadron operators, which are linear combinations of the single-hadron operators determined by solving a GEVP in the subspace created by the single-hadron operators. The two

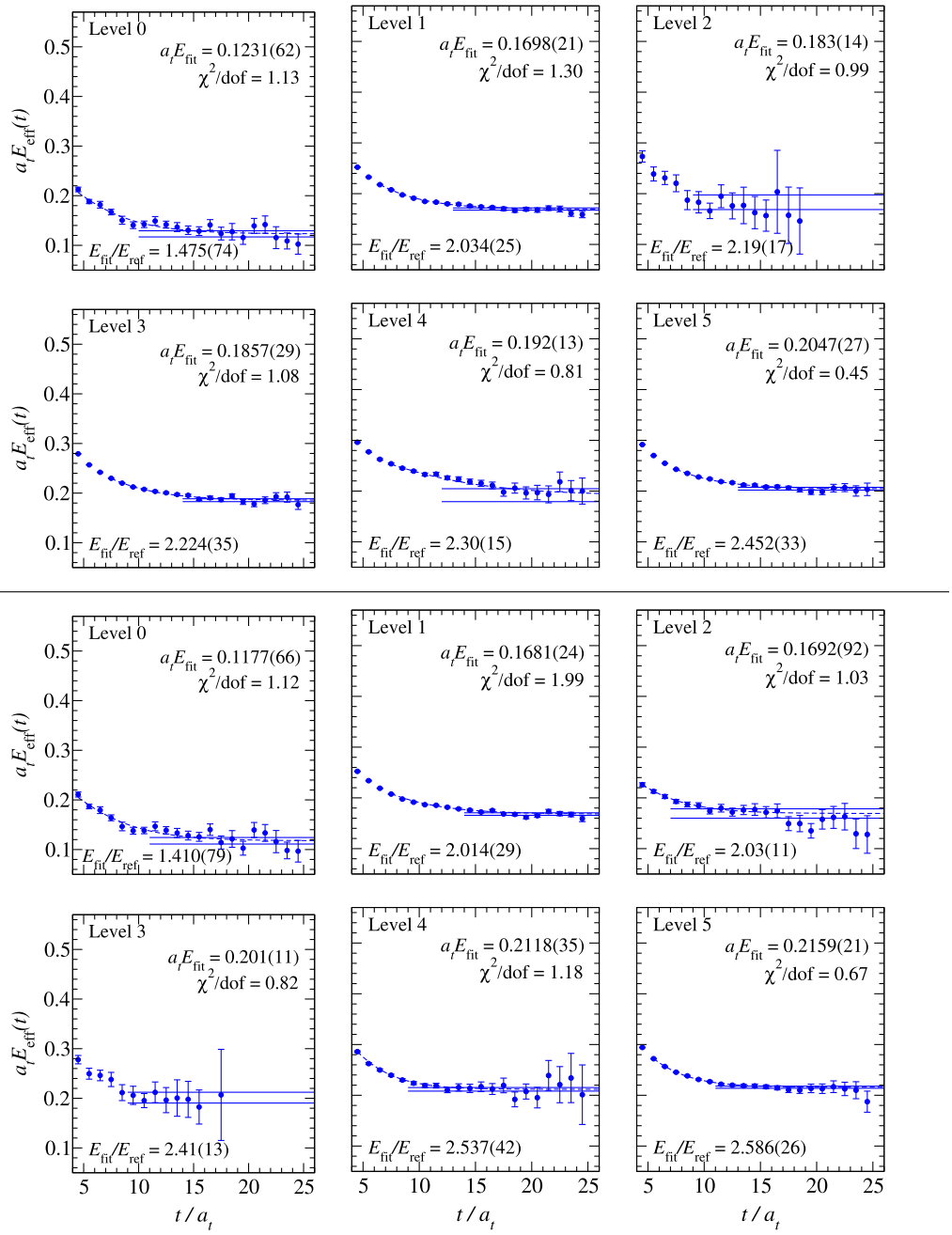


FIG. 7. Effective energies for the lowest six levels in the isotriplet, nonstrange, zero-momentum A_{1g}^- channel. Top two rows: results obtained using only the operators in Tables IV and V, excluding the tetraquark operator. Bottom two rows: results obtained using the operators in Tables IV and V and also including the tetraquark operator in Table VI. Effective energy curves calculated from correlator fits are overlaid, and fit results are shown.

single-hadron operators obtained in this way are denoted here by ROT 0 and ROT 1. The use of these operators in determining the overlap factors greatly aids in the level identifications. The overlap factors $|Z_j^{(n)}|^2$ are determined for all thirteen operators and are shown in Fig. 8. Each plot shows the factors for a single operator, with horizontal axis labeled by n, the index identifying the stationary states. Within each plot, the heights have been rescaled so that they add to unity, but keep in mind that overlaps with levels for $n \geq 13$ have not been determined.

First, consider the lowest-lying level 0. An inspection of the overlap plots in Fig. 8 shows that this state is predominantly created by the $\tilde{\eta}(0)\pi(0)$ and $\tilde{\phi}(0)\pi(0)$ operators. Given that our $\tilde{\eta}$ operator refers to $\bar{u}u + \bar{d}d$ and our $\tilde{\phi}$ operator is $\bar{s}s$, level 0 can be viewed as a state dominated by a pion at rest and a physical η at rest with

TABLE IX. Fit details for estimating the energies in the isotriplet nonstrange zero-momentum A_{1g}^- channel using the operator basis that excludes the tetraquark operator. See the caption of Table VII for further information about notation and headings.

E/E_K	a_tE	Fit model	$(\tau_{\min}, \tau_{\max})$	$\chi^2/N_{\rm dof}$
1.475(74)	0.1231(62)	2-exp	(3, 26)	1.13
2.034(25)	0.1698(21)	2-exp	(5, 26)	1.3
2.19(17)	0.183(14)	1-exp	(9, 26)	0.99
2.224(35)	0.1857(29)	2-exp	(6, 26)	1.08
2.30(15)	0.192(13)	2-exp	(6, 26)	0.81
2.452(33)	0.2047(27)	2-exp	(6, 26)	0.45
2.828(45)	0.2361(37)	2-exp	(6, 26)	0.71
2.971(32)	0.2480(26)	2-exp	(4, 26)	1.66
5.00(39)	0.417(33)	1-exp	(8, 18)	1.23

residual interactions. Next, consider stationary state level 1. This state is mainly created by the $\bar{K}(0)K(0)$ operator, so level 1 can be interpreted as a kaon-antikaon state with residual interactions. Levels 2 and 3 are produced mainly by the tetraquark and $\tilde{\phi}(0)\pi(0)$ operators, with small overlap factors from the $\tilde{\eta}(0)\pi(0)$ and ROT 0 operators. This leads to an identification of level 2 as predominantly a tetraquark state and level 3 as a $\pi\eta'$ state. Level 4 is mainly produced by the $\tilde{\phi}(1)\pi(1)$ operator, so can be interpreted as a pion and a physical η with back-to-back minimal relative momenta. Level 5 is mainly produced by the $\bar{K}(1)K(1)$ operator, so can be interpreted as a kaon-antikaon state having back-to-back minimal relative momenta.

A summary of the spectrum is shown in the center panel of Fig. 9, which is the analog of Fig. 6 in this channel. The nine lowest-lying energy estimates are indicated by the colored boxes, horizontally displaced for improved visibility. The horizontal gray line indicates the four-particle $\pi\pi\pi\eta$ threshold (there are no three-particle states in this channel in this energy range).

TABLE X. Fit details for estimating the energies in the isotriplet nonstrange zero-momentum A_{1g}^- channel using the operator basis that includes the tetraquark operator. See the caption of Table VII for further information about notation and headings.

E/E_K	a_tE	Fit model	$(\tau_{\min}, \tau_{\max})$	$\chi^2/N_{\rm dof}$
1.410(79)	0.1177(66)	2-exp	(3, 26)	1.12
2.014(29)	0.1681(24)	2-exp	(6, 26)	1.99
2.03(11)	0.1692(92)	2-exp	(3, 26)	1.03
2.41(13)	0.201(11)	1-exp	(9, 26)	0.82
2.537(42)	0.2118(35)	2-exp	(3, 26)	1.18
2.586(26)	0.2159(21)	2-exp	(4, 26)	0.67
2.84(12)	0.237(10)	2-exp	(3, 24)	0.99
2.947(40)	0.2461(33)	2-exp	(4, 26)	0.9
2.964(35)	0.2475(29)	2-exp	(4, 26)	1.64
5.01(39)	0.418(33)	1-exp	(8, 18)	1.25

The seven lowest-lying two-particle noninteracting energies are shown in the right panel of Fig. 9. For the noninteracting energies, η and ϕ refer to the physical particles, in contrast to our operator nomenclature. The lowest-lying level in the center panel corresponds to the $\pi(0)\eta(0)$ noninteracting state with a significant energy shift. In fact, fairly large energy shifts away from the noninteracting energies are observed for most of the levels.

The left panel in Fig. 9 shows our best attempt to extract the spectrum using the set of twelve operators in Tables IV and V which excludes the tetraquark operator. Note that including more single-hadron and two-meson operators does *not* change these extractions of the lowest-lying energies; we explicitly checked this in low-statistics calculations. The pattern of energies in the left panel differs dramatically from that in the center panel. Levels 0 and 1 agree fairly well, but the pattern is very different above these levels. Without the presence of the tetraquark in the left panel, some of the other operators which produce small overlap factors with level 2 must fill in the role of producing this level and simply cannot do so very well by a temporal separation of $t_{\max}$ in the correlators. The ROT 1 operator especially results in a large change to the extracted energies. Without the tetraquark operator in the left panel, one clearly sees that the remaining operators do a poor job of resolving the energy spectrum obtained in the middle panel. All of the single-meson and two-meson operators have very small overlap factors with stationary state 2 of the center panel and most have large overlap factors with the higher-lying states. Because of this, several extracted energies have very large errors and occur erroneously at values above that of stationary state 2 and below that of the higher states. This phenomenon, which occurs when a state is essentially missed by the entire operator set used, has been commonly known in lattice QCD since the first glueball calculations in the 1980s, but an explicit explanation can be found in Ref. [32]. In the center panel, the presence of the tetraquark operator dramatically improves the energy extractions. The purple hatched level 2 is reliably determined using the tetraquark operator, and the other operators can then focus on tending toward the levels corresponding to their largest overlap factors.

We conclude that the tetraquark operator is very important for obtaining a reliable estimate of the finite-volume spectrum in this channel for energies below 2.7 m_K. Without the tetraquark operator, the pattern of extracted energies above level 1 is simply incorrect. Exclusion of the tetraquark operator has a dramatic adverse impact on the extraction of the energy spectrum.

It is interesting to observe that our results shown in the left panel of Fig. 9, determined excluding the tetraquark operator, qualitatively agree with the results shown in Fig. 3 of Ref. [33] obtained also without any tetraquark operators, once adjustments for the different allowed momenta magnitudes are taken into account. The results in that work

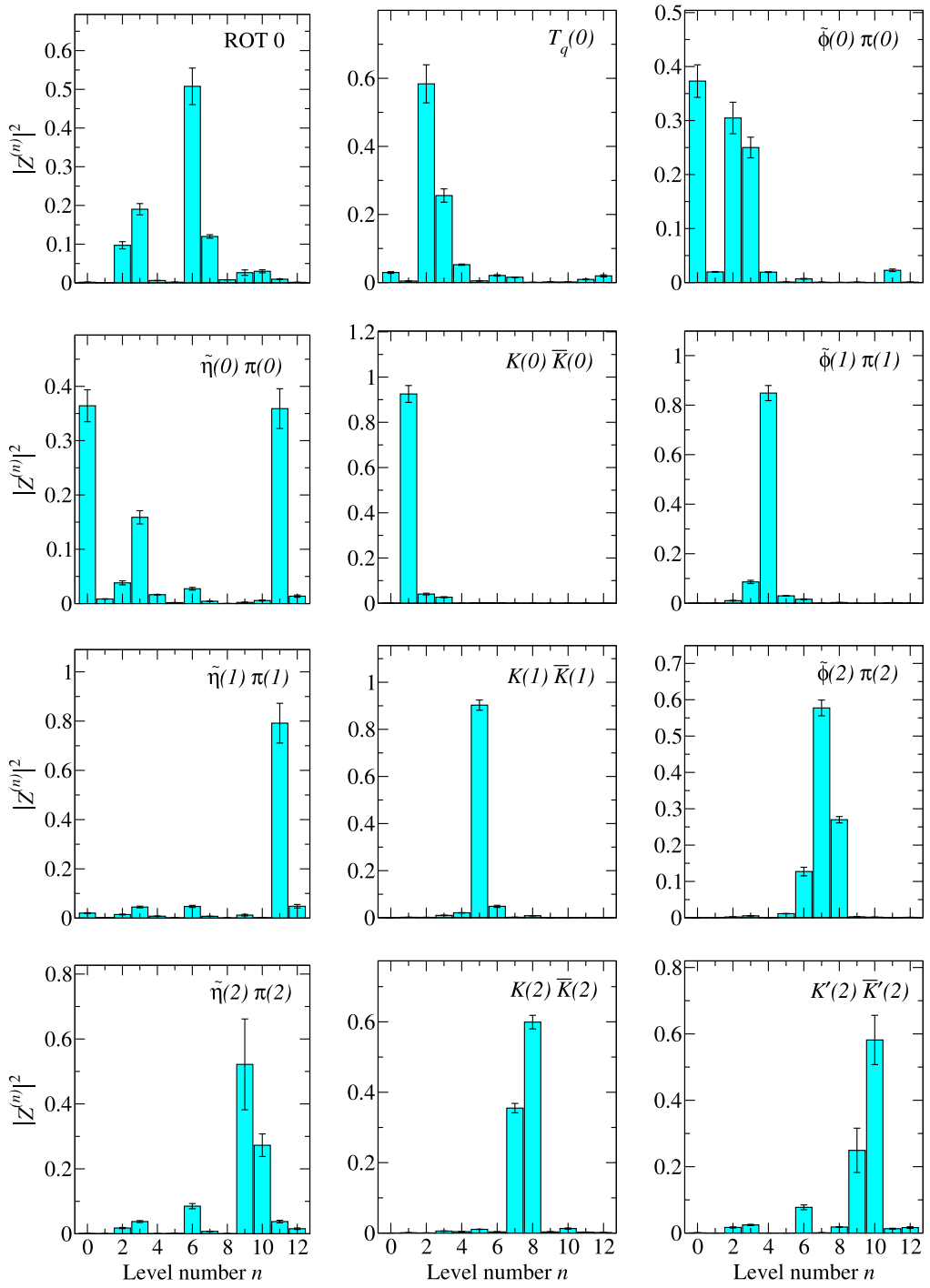


FIG. 8. Overlap factors $|Z_j^{(n)}|^2$ for twelve of the thirteen operators used in the correlator matrix corresponding to the isotriplet nonstrange zero-momentum A_{1g}^- channel. Each plot shows the factors for a single operator, with horizontal axis labeled by n, the index identifying the stationary states. The factors for the tetraquark operator are shown in the center plot in the top row. Operators labeled by `ROT N` denote our variationally improved single-hadron operators, as discussed in Sec. III C. $K(2), K'(2)$ refer to SS0, SS1 operators, respectively, and similarly for $\bar{K}(2), \bar{K}'(2)$ (see Table V). The factors for `ROT 1` (not shown) are all very small except for level 12.

were obtained using ensembles with the same lattice action but with $m_\pi \approx 400$ MeV and small spatial extents of 16, 20 and 24, as compared to 32 in this work. The overlap factors shown in Fig. 3 of Ref. [33] show significant mixings among nearly all of the different operators. As in the κ case, in the absence of the tetraquark operator, our overlap factors show a similar pattern, but this tendency disappears when the tetraquark operator is included, providing further

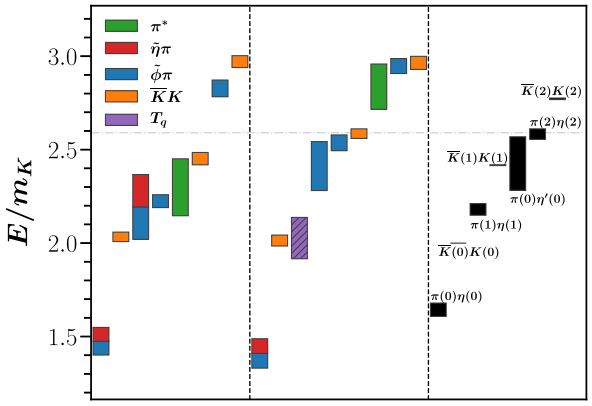


FIG. 9. Left: estimate of isotriplet, strangeness 0, zero-momentum, A_{1g}^- spectrum using operators in Tables IV and V, excluding the tetraquark operator. Center: estimate of the spectrum obtained using operators in Tables IV, V, and VI, which includes the tetraquark operator. Right: two-particle noninteracting energies. Statistical errors of the energy determinations are shown by the vertical extents of the boxes. The horizontal gray line indicates the four-particle $\pi\pi\pi\eta$ threshold (there are no three-particle states in this channel in this energy range). The flavor contents of the 13 basis operators are indicated by colors as shown in the legend. Levels predominantly created by a single operator are indicated by a single color corresponding to the flavor of the operator. Dual colored levels are predominantly created by two of the basis operators with comparable overlap factors. Levels created mostly by a single operator but with significant overlaps from one or more other operators are indicated by a hatched box.

evidence that without the tetraquark operator, the energy determinations become plagued by false plateaux which can lead to incorrect determinations of the overlap factors.

IV. SCATTERING AMPLITUDES

The last step in studying a resonance in lattice QCD is to apply the so-called Lüscher quantization condition using the finite-volume spectrum to determine the scattering K-matrix from which the resonance parameters can be deduced. Essentially, the goal is to apply a suitable parametrization of the K-matrix elements in terms of the center-of-mass energy and determine the best-fit values of the parameters by matching the energy spectra determined from the quantization condition in a finite volume to those obtained from the lattice QCD computations.

In this exploratory study, our goal is only to study the role of tetraquark operators in reliably computing the finite volume spectrum in lattice QCD in the channels associated with the κ and $a_0(980)$ resonances. For this reason, we simplify the computations by focusing only on the channels having zero total momentum. For a robust determination of the K-matrix, it is well known that it is best to use several total momenta. This is left for a future study. However, it is still interesting to examine the quantization condition with our results for zero total momentum.

This study employs a lattice of spatial volume L^3 and periodic spatial boundary conditions. The form of the quantization condition used here is given by

$$\det(\tilde{K}^{-1}(E_{\rm cm}) - B^{(\boldsymbol{P})}(E_{\rm cm})) = 0, \tag{19}$$

where $E_{\rm cm}$ denotes center-of-mass energy, $\tilde{K}(E_{\rm cm})$ is related to the usual scattering K-matrix as described below, and $B^{(\boldsymbol{P})}(E_{\rm cm})$ for a particular total momentum $\boldsymbol{P} = (2\pi/L)\boldsymbol{d}$, where $\boldsymbol{d}$ is a three-vector of integers, is the so-called "box matrix," using the notation of Ref. [34]. Equation (19) applies only for energies below all thresholds of states containing three or more particles. The determinant is taken over all unit normalized two-hadron states $|Jm_J\ell Sa\rangle$ specified by total angular momentum J, the projection of J along the z-axis m_J, the orbital angular momentum ℓ, the total intrinsic spin S, and particle species a.

Inserting the partial waves into the cubic box so as to maintain the periodic boundary conditions leads to the presence of the box matrix in Eq. (19). The elements $\langle J'm'_J\ell'S'a'|B^{(\boldsymbol{P})}(E_{\rm cm})|Jm_J\ell Sa\rangle$ of this matrix are given by known but complicated functions of some of the kinematic variables involved in the scattering process. This matrix is diagonal in the indices corresponding to total intrinsic spin and particle species, but not to any of the other indices. In particular, states of different total angular momentum can mix. It is straightforward to show that, under any symmetry transformation Q of the cubic box which is an element of the little group of $\boldsymbol{P}$, the box matrix transforms as $QB^{(\boldsymbol{P})}Q^\dagger = B^{(\boldsymbol{P})}$. This reveals that the box matrix can be block diagonalized by projecting onto the superpositions of states that transform according to the irreps of the little group. The $\tilde{K}$ matrix similarly block diagonalizes in such a basis, except for the total intrinsic spin and particle species indices. Hence, the determinant in Eq. (19) can be dealt with separately block by block. A particular block can be denoted by the finite-volume irrep $\Lambda(\boldsymbol{d}^2)$ and a row of this irrep λ. Since the spectrum is independent of the row λ, this index is henceforth omitted. For a particular block, the block-diagonalized box-matrix is denoted $B^{\Lambda(\boldsymbol{d}^2)}_{J'\ell'n';J\ell n}$, where n, n' are irrep occurrence numbers. The expressions for all elements of $B^{\Lambda(\boldsymbol{d}^2)}$ relevant for this work are given in Ref. [34]. After transforming to the block diagonal matrix, the $\tilde{K}$ matrix has the form given by Eq. (35) in Ref. [34]. A truncation $\ell \le \ell_{\rm max}$ in each block then makes the determinant condition manageable.

We use the same definition of the K-matrix as described in Ref. [34]. This matrix is real and symmetric and diagonal in total angular momentum and its projection

$$\langle J'm'_J\ell'S'a'|K|Jm_J\ell Sa\rangle = \delta_{J'J}\delta_{m'_Jm_J}K^{(J)}_{\ell'S'a';\ell Sa}(E_{\rm cm}). \tag{20}$$

The matrix $\tilde{K}$ here is defined by

$$\tilde{K}^{(J)-1}_{\ell' S' a';\ell S a}(E_{\rm cm}) = k_{a'}^{\ell'+\frac{1}{2}} K^{(J)-1}_{\ell' S' a';\ell S a}(E_{\rm cm}) k_a^{\ell+\frac{1}{2}}, \quad (21)$$

where

$$k_a^2 = \frac{1}{4}E_{\rm cm}^2 - \frac{1}{2}(m_{a_1}^2 + m_{a_2}^2) + \frac{(m_{a_1}^2 - m_{a_2}^2)^2}{4E_{\rm cm}^2}, \quad (22)$$

for a decay channel a involving particles of mass m_{a_1} and m_{a_2}. Note that this definition of $\tilde{K}$ differs very slightly from that given in Ref. [34], and hence, the box matrix here also is slightly different. Simple factors related to the spatial extent L have been removed here.

A. Scattering in the κ channel

In the isodoublet, strangeness 1, A_{1g} channel, there are two decay channels for any low-lying resonance: $K\pi$ and $K\eta$. The expansion in ℓ is known to converge very quickly. If we focus on the dominant $\ell = 0$ contribution, the quantization condition involves a 2×2 matrix for the two channels. The overlap factors show very little mixing between the $K\pi$ and $K\eta$ channels, and this is also observed experimentally for the $K_0^*(700)$ resonance, which decays overwhelmingly to $K\pi$ [35]. This means the off-diagonal elements of the matrix whose determinant appears in the quantization condition in Eq. (19) can be taken to be negligible to a good approximation, and the quantization condition simplifies to an equality with zero of a product of two separate scalar functions.

The quantization condition for the $K\pi$ channel is studied in Fig. 10. The black curve in this figure shows the box matrix $B^{(\boldsymbol{P})}$ as a function of $E_{\rm cm}/m_K$ using the mean values of the kaon and pion masses, as well as the mean value determined for the lattice anisotropy, as presented in Table III. The singularities of this function at the noninteracting energies are indicated by the vertical dashed lines. The intersections of the $\tilde{K}^{-1}$ curve with the black curve satisfy the quantization condition. The goal is to find a parametrization of $\tilde{K}^{-1}$ that produces intersections with the black curve at the energies shown by the red points in the lower panel, which are the energies obtained in our lattice QCD computations that correspond to the $K\pi$ channel (the red blocks of levels 0, 1, and 4 in the center panel of Fig. 6). The blue and orange curves show the best fits when $\tilde{K}^{-1}$ is taken to be a constant and linear function, respectively. In this energy range, the best-fit constant and linear functions intersect with the black curve at three energies, but these energies do not agree well with the energies in the lower panel, as indicated by the large values of chi-square per degree of freedom shown in the legend. The χ^2 used here to compute the fit qualities are defined using the differences in the finite-volume $E_{\rm cm}/m_K$ values obtained from the quantization condition and the lattice determinations as the residuals, taking all covariances into account, except neglecting the small uncertainties in the

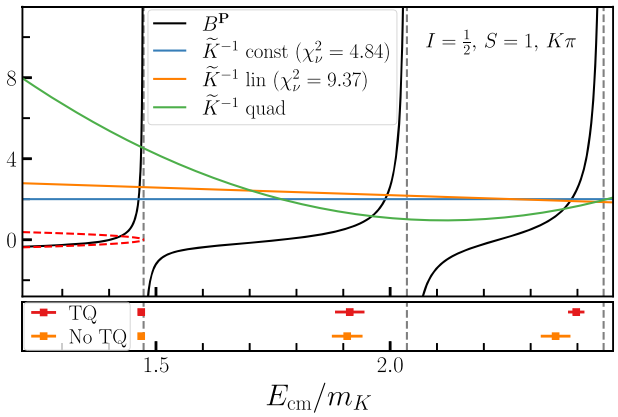


FIG. 10. Study of the Lüscher quantization condition for the $I = \frac{1}{2}, S = 1, A_{1g}$ channel with zero total momentum, restricted to relative orbital angular momentum $\ell = 0$ and the $K\pi$ decay channel. Upper panel: the black curve shows the box matrix $B^{(\boldsymbol{P})}$ function against center-of-mass energy over kaon mass, with its singularities at the noninteracting energies indicated by vertical dashed lines. Blue, orange, and green curves show the behavior of $\tilde{K}^{-1}$ for constant, linear, and quadratic forms, respectively. Intersections of these curves with the black curves indicate the energies that satisfy the quantization condition. Vertical dashed lines indicate the noninteracting energies, and the red dashed curve is $\pm\sqrt{-(k_{K\pi}/m_K)^2}$. In the legend, $\chi^2_\nu = \chi^2/N_{\rm dof}$. Lower panel: finite-volume energies for the predominantly $K\pi$ states from the lattice QCD computations which include (exclude) the tetraquark operator are shown by the red (orange) points.

single-meson masses. The green curve shows that a quadratic function of $E_{\rm cm}/m_K$ for $\tilde{K}^{-1}$ is able to intersect the black curve at the energies shown in the lower panel reasonably well. With only three energies in this channel of zero total momentum and three parameters in the function to be fit, there are zero degrees of freedom in such a fit, so additional total momenta are needed to reliably determine this function. The main point to be made here, however, is that the tetraquark operator appears to play no role in the $K\pi$ channel, so the omission of the tetraquark operator does not adversely affect any lattice QCD study of the κ resonance.

The quantization condition for the $K\eta$ channel is studied in Fig. 11. The black curve in this figure again shows the box matrix $B^{(\boldsymbol{P})}$ as a function of $E_{\rm cm}/m_K$ using the mean values of the kaon and η masses and the lattice anisotropy. In the lower panel, the red points show the energies of levels 2, 3, and 5 in the center panel of Fig. 6, obtained in the lattice QCD computations including a tetraquark operator. The orange points in the lower panel show the energies extracted when the tetraquark operator is excluded in the analysis. The blue and orange curves show the best fits when $\tilde{K}^{-1}$ is taken to be a constant and linear function, respectively. In this energy range, the best-fit constant and linear functions intersect with the black curve at three energies. The intersections

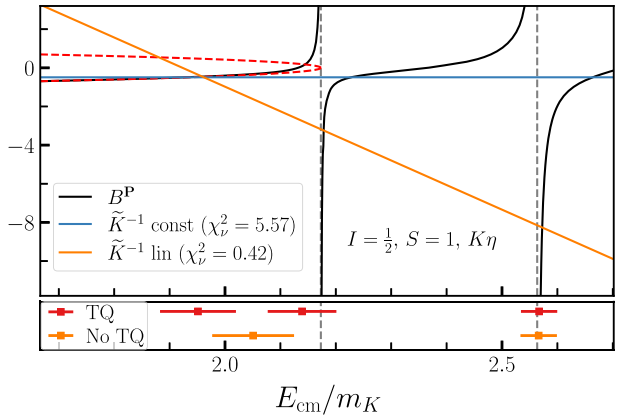


FIG. 11. Study of the Lüscher quantization condition for the $I = \frac{1}{2}, S = 1, A_{1g}$ channel with zero total momentum, restricted to relative orbital angular momentum $\ell = 0$ and the $K\eta$ decay channel. Upper panel: the black curve shows the box matrix $B^{(\boldsymbol{P})}$ function against center-of-mass energy over kaon mass, with its singularities at the noninteracting energies indicated by vertical dashed lines. Blue and orange curves show the behavior of $\tilde{K}^{-1}$ for constant and linear forms, respectively. Intersections of these curves with the black curves indicate the energies that satisfy the quantization condition. Vertical dashed lines indicate the noninteracting energies, and the red dashed curve is $\pm\sqrt{-(k_{K\pi}/m_K)^2}$. In the legend, $\chi^2_\nu = \chi^2/N_{\rm dof}$. Lower panel: finite-volume energies for the predominantly $K\eta$ states from the lattice QCD computations which include (exclude) the tetraquark operator are shown by the red (orange) points.

with the constant function do not agree very well with the red points in the lower panel below, but the energies from the linear function do.

Without the tetraquark operator, only two intersections with the black curve would be allowed in order to agree with the orange points. Figure 11 illustrates how difficult it would be to find a suitable form for $\tilde{K}^{-1}$ that could accomplish only two intersections which agree with the orange points. This is further evidence that the analysis excluding the tetraquark operator has led to missing an important energy level. Moreover, under the assumption of a decoupled $K\eta$ channel, the intersections of the $\tilde{K}^{-1}$ curves with the dashed red line in Fig. 11 suggest the existence of a bound $K\eta$ state when the analysis includes the tetraquark operator. Recall that $k\cot\delta_0(k) = \varepsilon\sqrt{-k^2}$ is the S-wave bound state condition for $\varepsilon = -1$ and the S-wave virtual bound state condition for $\varepsilon = +1$. Without the tetraquark operator, such intersections seem unlikely to occur, leading to an absence of any bound state. We emphasize the qualitative nature of our analysis, noting that a quantitative study of $\tilde{K}^{-1}$ would require many more energy levels using a variety of different total momenta.

Although the absence of the tetraquark operator does not adversely impact a study of the κ resonance, the $K_0^*(1430)$ decays to both $K\pi$ and $K\eta$, so a missed low-lying state in the $K\eta$ channel could adversely impact a study of this resonance.

B. Scattering in the $a_0(980)$ channel

For the configuration ensemble used in this study, the π, K, η, η' are all stable against strong decays. Hence, in the isotriplet, strangeness 0, A_{1g}^- channel, there are three decay channels for any low-lying resonance: $\bar{K}K$, $\pi\eta$, and $\pi\eta'$. The expansion in ℓ is known to converge very quickly. If we focus on the dominant $\ell = 0$ contribution, the quantization condition involves a 3×3 matrix for the three channels. When the tetraquark operator is included in the analysis, the overlap factors show very little mixing among the $\bar{K}K$, $\pi\eta$, and $\pi\eta'$ decay channels. Also, in Ref. [35], the branching ratio of decays of the $a_0(980)$ to $\bar{K}K$ over that of $\pi\eta$ is about 0.17, and the branching ratio to $\pi\eta'$ decays over total decays is very small. These facts suggest that the off-diagonal elements of the matrix whose determinant appears in the quantization condition of Eq. (19) should be negligible to a good approximation, and so, the quantization condition simplifies to an equality with zero of a product of three separate scalar functions.

The quantization condition for the $\pi\eta$ channel is studied in Fig. 12. The black curve in this figure shows the box matrix $B^{(\boldsymbol{P})}$ function as a function of $E_{\rm cm}/m_K$ using the mean values of the pion and η masses and the lattice anisotropy. In the lower panel, the red points show the energies of levels 0, 2, and 4 in the center panel of Fig. 9, obtained in the lattice QCD computations with the inclusion of a tetraquark operator. The $\bar{K}K$ energies of levels 1 and 5, indicated by the orange boxes in Fig. 9, are excluded in the lower panel of Fig. 12. The energy of level 3 is also excluded since overlap factors suggest this level is predominantly a $\pi\eta'$ state. The orange points in the lower panel show the energies extracted when the tetraquark operator is excluded in the analysis.

Without the tetraquark operator, the overlap factors erroneously show much more mixing, making it difficult to identify the state which is predominantly the $\pi\eta'$ state. In the lower panel, we select one of two states which we believe have significant overlap with the $\pi\eta'$ so at least the number of states is correct. The blue and orange curves show the best fits when $\tilde{K}^{-1}$ is taken to be a constant and linear functions, respectively. The green curve is a quadratic function engineered to intersect the black curve at energies within the red error bars; with zero degrees of freedom, it is not a fit. In this energy range, the best-fit constant and linear functions intersect with the black curve at three energies. The intersections with the constant and linear functions do not agree very well with the red points in the lower panel below, as indicated by the large $\chi^2/N_{\rm dof}$ values of the fits. To achieve a reasonably good matching of the three

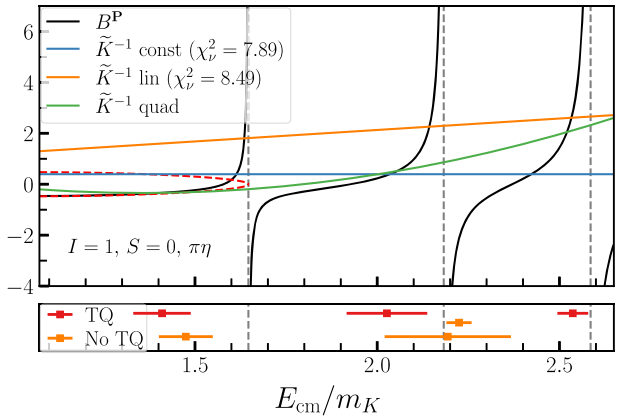


FIG. 12. Study of the Lüscher quantization condition for the $I = 1, S = 0, A_{1g}^-$ channel with zero total momentum, restricted to relative orbital angular momentum $\ell = 0$ and the $\pi\eta$ decay channel. Upper panel: the black curve shows the box matrix $B^{(\boldsymbol{P})}$ function against center-of-mass energy over kaon mass, with its singularities at the noninteracting energies indicated by vertical dashed lines. Blue, orange, and green curves show the behavior of $\tilde{K}^{-1}$ for constant, linear, and quadratic forms, respectively. Intersections of these curves with the black curves indicate the energies that satisfy the quantization condition. Vertical dashed lines indicate the noninteracting energies, and the red dashed curve is $\pm\sqrt{-(k_{\pi\eta}/m_K)^2}$. In the legend, $\chi^2_\nu = \chi^2/N_{\rm dof}$. Lower panel: finite-volume energies for the predominantly $\pi\eta$ states (see text) from the lattice QCD computations which include (exclude) the tetraquark operator are shown by the red (orange) points.

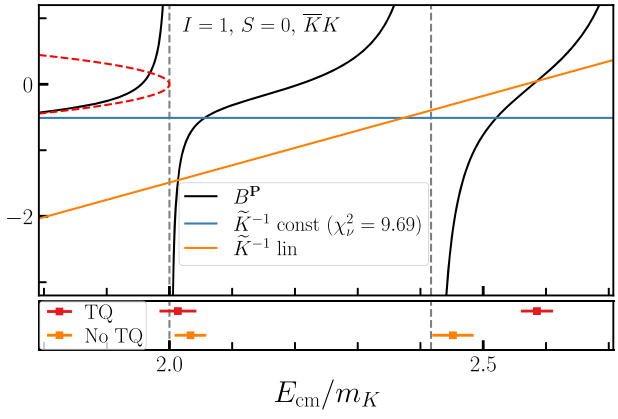


FIG. 13. Study of the Lüscher quantization condition for the $I = 1, S = 0, A_{1g}^-$ channel with zero total momentum, restricted to relative orbital angular momentum $\ell = 0$ and the $\bar{K}K$ decay channel. Upper panel: the black curve shows the box matrix $B^{(\boldsymbol{P})}$ function against center-of-mass energy over kaon mass, with its singularities at the noninteracting energies indicated by vertical dashed lines. Blue and orange curves show the behavior of $\tilde{K}^{-1}$ for constant and linear forms, respectively. Intersections of these curves with the black curves indicate the energies that satisfy the quantization condition. Vertical dashed lines indicate the noninteracting energies, and the red dashed curve is $\pm\sqrt{-(k_{\bar{K}K}/m_K)^2}$. In the legend, $\chi^2_\nu = \chi^2/N_{\rm dof}$. Lower panel: finite-volume energies for the predominantly $\bar{K}K$ states from the lattice QCD computations which include (exclude) the tetraquark operator are shown by the red (orange) points.

intersections with the red points in the lower panel, it appears that a function with some curvature, such as a quadratic function, is needed. Without the tetraquark operator, Fig. 12 shows that matching the intersections with the orange points would lead to a dramatically different $\tilde{K}^{-1}$, requiring significant downward curvature on the right to intersect the right most section of the black curve at a significantly lower energy.

The quantization condition for the $\bar{K}K$ channel is studied in Fig. 13. The black curve in this figure shows the box matrix $B^{(\boldsymbol{P})}$ function as a function of $E_{\rm cm}/m_K$ using the mean values of the kaon and η masses and the lattice anisotropy. In the lower panel, the red points show the energies of levels 1 and 5 in the center panel of Fig. 9, obtained in the lattice QCD computations with the inclusion of tetraquark operators. The orange points in the lower panel show the energies for the $\bar{K}K$ dominated states extracted when the tetraquark operator is excluded in the analysis. The blue curve shows the best fit when $\tilde{K}^{-1}$ is taken to be a constant function. The orange curve is a linear function engineered to intersect the black curve at energies within the red error bars; with zero degrees of freedom, it is not a fit. In this energy range, the best-fit constant and the linear functions intersect with the black curve at two energies. The intersections with the constant function do not agree very well with the red points in the lower panel below, as indicated by the large $\chi^2/N_{\rm dof}$ values of the fit. To achieve a reasonably good matching of the two intersections with the red points in the lower panel, the linear function is needed. Without the tetraquark operator, Fig. 13 shows that matching the intersections with the orange points would lead to a linear function for $\tilde{K}^{-1}$ with a dramatically different slope.

V. CONCLUSION

Due to the manner in which stationary-state energies are extracted from matrices of temporal correlations of single- and multihadron operators in lattice QCD, the unfortunate possibility exists of flawed spectrum extractions whenever an operator set is insufficient to provide overlaps onto all relevant finite-volume stationary states. In this work, the isodoublet, strangeness 1, zero-momentum, A_{1g} channel relevant for the κ resonance and the isotriplet nonstrange zero-momentum A_{1g}^- channel relevant for the $a_0(980)$ channel were studied. We found that in both cases, neglecting to include a particular type of tetraquark operator in the correlator matrices led to a flawed energy spectrum extraction. The impact of these erroneous energies on determinations of scattering amplitudes and

resonance parameters using the Lüscher quantization condition was studied in both case.

In the $I = \frac{1}{2}, S = 1$ case, the energies of states dominated by $K\eta$ pairs were significantly impacted, with one level completely missed when the tetraquark was excluded from the analysis, whereas the $K\pi$ energies were only slightly affected. Since the κ resonance decays primarily to $K\pi$ states, omission of a tetraquark operator does not appear to adversely impact studies of the κ resonance. However, this work suggests that the use of a tetraquark operator will be important for any lattice QCD study of the $K_0^*(1430)$ resonance.

In the $I = 1$, $S = 0$ case, omission of a tetraquark operator led to substantial changes in the energies. This strongly suggests that lattice QCD studies of the $a_0(980)$ resonance can obtain reliable results only if a tetraquark operator of the type described in this work is included in the analysis.

The results of this work underscore the importance of including tetraquark operators in studying low-lying mesonic resonances, such as the $a_0(980)$. This exploratory investigation focused only on correlator matrices involving states of total zero momentum. Future work will include increased statistics, channels involving several nonzero total momenta, as well as a variety of different lattice volumes and lattice spacings. The importance of tetraquark operators in lattice QCD studies of other light meson resonances, such as the isoscalar σ, should also be investigated.

ACKNOWLEDGMENTS

We acknowledge helpful discussions with Ben Hörz. Computations were carried out at the Oak Ridge Leadership Computing facility at Oak Ridge National Laboratory and on Frontera [36] at the Texas Advanced Computing Center (TACC). Our software to evaluate the correlators made use of the CHROMA [37] library. C. M., J. M., and S. S. acknowledge support from the U.S. National Science Foundation (NSF) under Awards No. PHY-2209167 and No. PHY-2514831. NSF Awards No. PHY-1306805 and No. PHY-1613449 supported A. D. H., J. F., R.B, and D. D. during early stages of this investigation. Any opinions, findings, and conclusions or recommendations expressed in this material are those of the author(s) and do not necessarily reflect the views of the National Science Foundation. This work was also supported by the U.S. Department of Energy (DOE), Office of Science, Office of Nuclear Physics, under grant contract number DE-AC02-05CH11231 (A. W. L.). The work of F. R. L. was supported in part by the Swiss National Science Foundation (SNSF) through Grant No. 200021-236432. J. B. is supported by the European Research Council (ERC) consolidator Grant No. StrangeScatt-101088506.

DATA AVAILABILITY

There are no publicly available research data or software supporting this manuscript. Requests for further information or data should be sent to the authors.

[1] S. Godfrey and N. Isgur, Mesons in a relativized quark model with chromodynamics, Phys. Rev. D **32**, 189 (1985).
[2] G. Rupp and E. Van Beveren, Scalar mesons: Fifty years of challenging the quark model, Acta Phys. Pol. B Proc. Suppl. **11**, 455 (2018).
[3] R. Jaffe, Exotica, Nucl. Phys. B, Proc. Suppl. **142**, 343 (2005).
[4] C. Amsler and N. Tornqvist, Mesons beyond the naive quark model, Phys. Rep. **389**, 61 (2004).
[5] F. E. Close and N. A. Tornqvist, Scalar mesons above and below 1 GeV, J. Phys. G **28**, R249 (2002).
[6] L. Maiani, F. Piccinini, A. Polosa, and V. Riquer, New look at scalar mesons, Phys. Rev. Lett. **93**, 212002 (2004).
[7] A. Stump and J. R. Green, Position-space sampling for local multiquark operators in lattice QCD using distillation and the importance of tetraquark operators for $T_{cc}(3875)^+$, Phys. Rev. D **113**, 034513 (2026).
[8] S. Prelovsek, E. Ortiz-Pacheco, S. Collins, L. Leskovec, M. Padmanath, and I. Vujmilovic, Doubly heavy tetraquarks from lattice QCD: Incorporating diquark-antidiquark operators and the left-hand cut, Phys. Rev. D **112**, 014507 (2025).
[9] H. Alharazin, A. B. Raposo, J. Bulava, S. Dawid, J. R. Green, C. Morningstar, F. Romero-López, M. Salg, S. R. Sharpe, and A. Stump, Three-body study of the $T_{cc}(3875)^+$ from lattice QCD, in *42th International Symposium on Lattice Field Theory* (2026), arXiv:2602.17204.
[10] S. Prelovsek, T. Draper, C. B. Lang, M. Limmer, K.-F. Liu, N. Mathur, and D. Mohler, Lattice study of light scalar tetraquarks with $I = 0, 2, 1/2, 3/2$: Are σ and κ tetraquarks?, Phys. Rev. D **82**, 094507 (2010).
[11] C. Alexandrou, J. O. Daldrop, M. Dalla Brida, M. Gravina, L. Scorzato, C. Urbach, and M. Wagner, Lattice investigation of the scalar mesons $a_0(980)$ and κ using four-quark operators, J. High Energy Phys. 04 (2013) 137.
[12] C. Alexandrou, J. Berlin, M. Dalla Brida, J. Finkenrath, T. Leontiou, and M. Wagner, Lattice QCD investigation of the structure of the $a_0(980)$ meson, Phys. Rev. D **97**, 034506 (2018).
[13] F.-K. Guo, L. Liu, U.-G. Meissner, and P. Wang, Tetraquarks, hadronic molecules, meson-meson scattering and disconnected contributions in lattice QCD, Phys. Rev. D **88**, 074506 (2013).

[14] C. Morningstar, J. Bulava, J. Foley, K. J. Juge, D. Lenkner, M. Peardon, and C. H. Wong, Improved stochastic estimation of quark propagation with Laplacian Heaviside smearing in lattice QCD, Phys. Rev. D **83**, 114505 (2011).
[15] M. Luscher, Two particle states on a torus and their relation to the scattering matrix, Nucl. Phys. **B354**, 531 (1991).
[16] K. Rummukainen and S. A. Gottlieb, Resonance scattering phase shifts on a nonrest frame lattice, Nucl. Phys. **B450**, 397 (1995).
[17] C. H. Kim, C. T. Sachrajda, and S. R. Sharpe, Finite-volume effects for two-hadron states in moving frames, Nucl. Phys. **B727**, 218 (2005).
[18] R. A. Briceno, Two-particle multichannel systems in a finite volume with arbitrary spin, Phys. Rev. D **89**, 074507 (2014).
[19] G. Fox, R. Gupta, O. Martin, and S. Otto, Monte Carlo estimates of the mass gap of the O(2) and O(3) spin models in $(1+1)$-dimensions, Nucl. Phys. **B205**, 188 (1982).
[20] C. Michael and I. Teasdale, Extracting glueball masses from lattice QCD, Nucl. Phys. **B215**, 433 (1983).
[21] M. Lüscher and U. Wolff, How to calculate the elastic scattering matrix in two-dimensional quantum field theories by numerical simulation, Nucl. Phys. **B339**, 222 (1990).
[22] S. Basak, R. Edwards, G. Fleming, U. Heller, C. Morningstar, D. Richards, I. Sato, and S. Wallace, Group-theoretical construction of extended baryon operators in lattice QCD, Phys. Rev. D **72**, 094506 (2005).
[23] C. Morningstar, J. Bulava, B. Fahy, J. Foley, Y. Jhang, K. Juge, D. Lenkner, and C. Wong, Extended hadron and two-hadron operators of definite momentum for spectrum calculations in lattice QCD, Phys. Rev. D **88**, 014511 (2013).
[24] C. Morningstar and M. J. Peardon, Analytic smearing of SU(3) link variables in lattice QCD, Phys. Rev. D **69**, 054501 (2004).
[25] R. G. Edwards, B. Joo, and H.-W. Lin, Tuning for three-flavors of anisotropic clover fermions with stout-link smearing, Phys. Rev. D **78**, 054501 (2008).
[26] H.-W. Lin *et al.* (Hadron Spectrum Collaboration), First results from $2+1$ dynamical quark flavors on an anisotropic lattice: Light-hadron spectroscopy and setting the strange-quark mass, Phys. Rev. D **79**, 034502 (2009).
[27] R. Brett, J. Bulava, J. Fallica, A. Hanlon, B. Hörz, and C. Morningstar, Determination of s- and p-wave $I=1/2$ $K\pi$ scattering amplitudes in $N_{\mathrm{f}}=2+1$ lattice QCD, Nucl. Phys. **B932**, 29 (2018).
[28] J. Bulava, B. Fahy, B. Hörz, K. J. Juge, C. Morningstar, and C. H. Wong, $I=1$ and $I=2$ $\pi-\pi$ scattering phase shifts from $N_{\mathrm{f}}=2+1$ lattice QCD, Nucl. Phys. **B910**, 842 (2016).
[29] See Supplemental Material at http://link.aps.org/supplemental/10.1103/bs45-shv9 for further details about our tetraquark operator selection procedure.
[30] D. J. Wilson, J. J. Dudek, R. G. Edwards, and C. E. Thomas, Resonances in coupled $\pi K, \eta K$ scattering from lattice QCD, Phys. Rev. D **91**, 054008 (2015).
[31] G. Rendon, L. Leskovec, S. Meinel, J. Negele, S. Paul, M. Petschlies, A. Pochinsky, G. Silvi, and S. Syritsyn, $I=1/2$ S-wave and P-wave $K\pi$ scattering and the κ and K^* resonances from lattice QCD, Phys. Rev. D **102**, 114520 (2020).
[32] J. J. Dudek, R. G. Edwards, and C. E. Thomas (Hadron Spectrum Collaboration), Energy dependence of the ρ resonance in $\pi\pi$ elastic scattering from lattice QCD, Phys. Rev. D **87**, 034505 (2013); **90**, 099902(E) (2014).
[33] J. J. Dudek, R. G. Edwards, and D. J. Wilson (Hadron Spectrum Collaboration), An a_0 resonance in strongly coupled $\pi\eta$, $K\bar{K}$ scattering from lattice QCD, Phys. Rev. D **93**, 094506 (2016).
[34] C. Morningstar, J. Bulava, B. Singha, R. Brett, J. Fallica, A. Hanlon, and B. Hörz, Estimating the two-particle K-matrix for multiple partial waves and decay channels from finite-volume energies, Nucl. Phys. **B924**, 477 (2017).
[35] S. Navas *et al.* (Particle Data Group Collaboration), Review of particle physics, Phys. Rev. D **110**, 030001 (2024).
[36] D. Stanzione, J. West, R. Evans, T. Minyard, O. Ghattas, and D. Panda, Frontera: The evolution of leadership computing at the National Science Foundation, in *Proceedings of Practice and Experience in Advanced Research Computing (PEARC '20)* (Association for Computing Machinery (ACM), New York, NY, USA, 2020).
[37] R. G. Edwards and B. Joo (SciDAC Collaboration), The Chroma software system for lattice QCD, Nucl. Phys. B, Proc. Suppl. **140**, 832 (2005).